ACS OMEGA

Open Access

http://pubs.acs.org/journal/acsodf

Article

Role of Zn in the Microstructure, Segregation, and Cytotoxicity of Sn-0.2 Ni Solders

Jeverton Laureano Paixão, Raí Batista de Sousa, Pâmella Raffaela Dantas de Freitas, Rubiamara Mauricio de Sousa, Jefferson Romáryo Duarte da Luz, Bismarck Luiz Silva, and José Eduardo Spinelli*

Cite This: *ACS Omega* 2024, 9, 8829−8845

Read Online

ACCESS | Metrics & More | Article Recommendations

ABSTRACT: Sn−Ni system alloys are promising alternatives to replace Sn−Pb alloys as they exhibit high corrosion resistance and good weldability. However, Sn−Ni alloys still have low mechanical strength and low reliability. Using the strategy of the addition of alloying elements can be a way to improve the properties of Sn−Ni alloys. Zinc (Zn) plays an essential role in the lead-free solder alloys sector by mitigating the growth of intermetallic compounds in soldered joints, refining the microstructure, enhancing the mechanical strength, and ultimately reducing the overall cost. This study aims to explore the impacts of Zn additions (0.2 and 0.5 wt %) on thermal parameters (growth rate-V and cooling rate-$\dot{T}$), macrostructure, microstructure, phase transformation, macrosegregation, and cytotoxicity. All of these factors will be examined in directionally solidified Sn-0.2 wt % Ni alloys under transient heat flow conditions on a copper sheet. The samples underwent characterization using optical microscopy, scanning electron microscopy, X-ray fluorescence, and X-ray diffraction. Property diagrams and isopleths were generated by using the CALPHAD method. Cytotoxicity analysis involved assessing cell viability after 15 and 30 days of incubation for the alloys, followed by exposure of the extracts for 24 and 48 h. The Zn additions caused a significant increase in the melting temperature in the Sn−Ni−Zn alloys. Fully columnar macrostructures were observed for the Sn−Ni−Zn alloys. The as-cast microstructures of Sn−Ni−Zn alloys were completely dendritic, with an Sn-rich matrix (Sn-β) surrounded by a Ni_3Sn_4 + NiSn + Sn-β phase eutectic mixture. Zn additions did not change the dendritic arrangement of the Sn−Ni−Zn alloys when compared to the Sn-0.2 wt % Ni. Furthermore, increasing the Zn content did not affect the microstructural scale in the ternary Sn−Ni−Zn alloys. The toxicity of the examined alloys is not significantly influenced by the microstructural length scale. On the other hand, factors such as incubation time and chemical composition may have an impact on the cytotoxicity. Overall, the presence of Zn in the Sn−Ni−Zn alloys enhanced the cell viability.

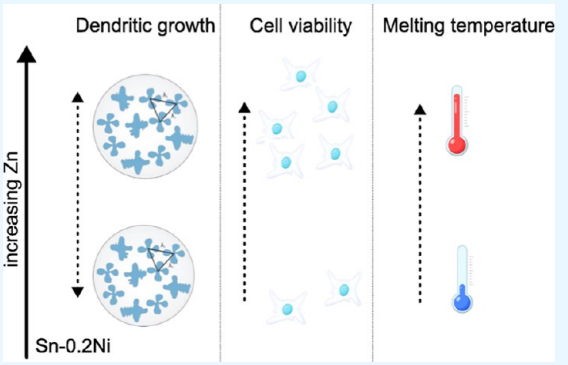

1. INTRODUCTION

Materials with suitable mechanical, electrical, and thermal properties for applications in soldered joints are urgent in the context of the electronics industry, which requires high performance and sustainability. In this context, lead-free alloys appear. Such alloys need to have similar properties as compared to Sn−Pb alloys, however with lower levels of toxicity, higher reliability, affordable cost, and good resistance to thermomechanical fatigue.[1−3]

Lead-free soldering tin-based alloys have been proposed in the last years, especially Sn−Ni alloys, maintained as binary or modified with additional alloying.[4,5] Binary Sn−Ni alloys have a high potential for application in electronic components due to their suitable corrosion resistance and good weldability, in addition to their hypereutectic, eutectic, and hypoeutectic compositions requiring low levels of Ni, which is a cost advantage.[6] According to the literature, the eutectic reaction of the Sn−Ni system at equilibrium is L (liquid) → (Sn) + Ni_3Sn_4, and Ni has negligible solubility in Sn at 231.15 °C.[7] Ni is widely used in electronic packaging, where it is generally used as a solder barrier between Cu and solder alloy because of its slower reaction rate compared to the reaction kinetics between Sn and Cu.[8] Furthermore, Ni has been added as a third or fourth element in Sn-based alloys.[9−11]

The improvement of a lead-free alloy for electronic packaging has been mostly achieved through the microaddition of elements. This technique can significantly impact micro-

Received: August 24, 2023
Revised: December 14, 2023
Accepted: January 8, 2024
Published: February 16, 2024

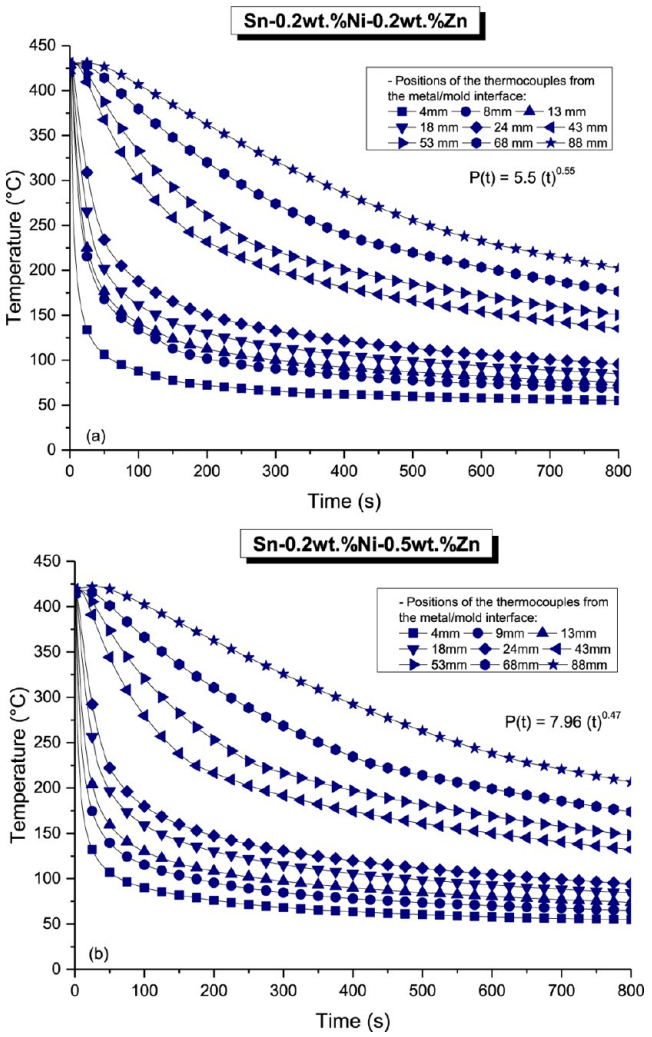

Figure 1. Thermal profiles along the length of the (a) Sn-0.2 wt % Ni-0.2 wt % Zn and (b) Sn-0.2 wt % Ni-0.5 wt % Zn solder alloys.

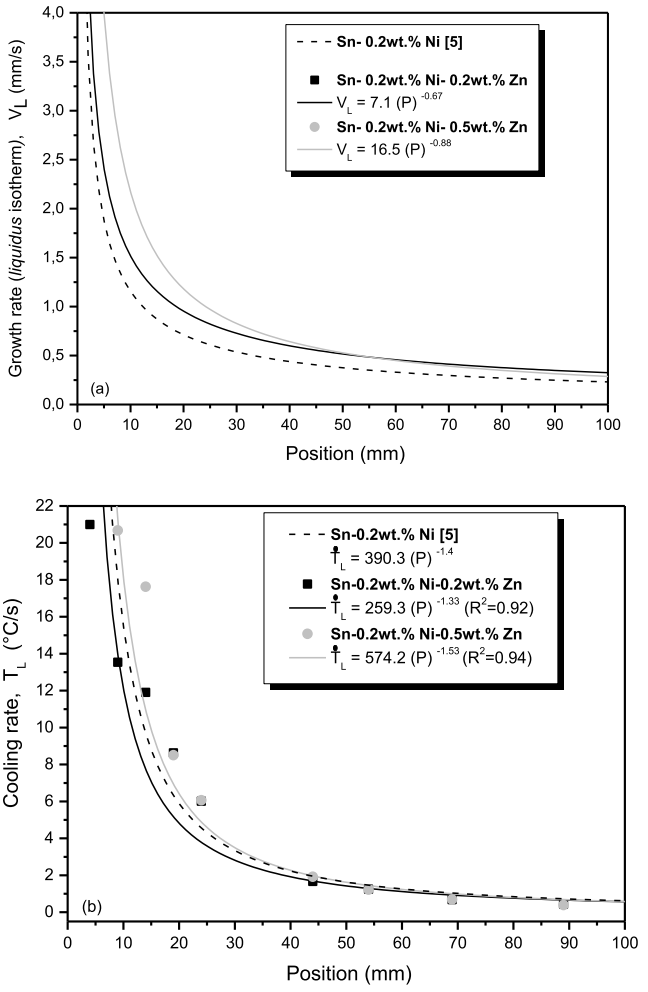

Figure 2. Variation of the thermal parameters for the Sn-0.2 wt % Ni-0.2 wt % Zn and Sn-0.2 wt % Ni-0.5 wt % Zn solders: (a) growth rate (V_L) and (b) cooling rate ($\dot{T}_L$) as a function of position (P) from the metal/mold plate interface.

structural refinement and enhancements in physical or functional behavior even with very little addition.[12,13] Nevertheless, research on how microadditions of alloying elements, such as Zn, affect the eutectic Sn−Ni structure, segregation, phase formation, and mechanical and physical properties has not yet been covered in the literature. Zn presents a compelling substitute as a ternary alloying element due to its inherent low cost. Zinc also serves as a microstructure refiner, enhancing the mechanical properties and preventing the segregation of other alloying elements.[8,14,15]

The absence of studies in the literature examining relationships between the ternary Sn−Ni−Zn alloys' microstructure, cooling rate, and mechanical properties strengthens the need for the present investigation.

Investigations on the toxicity of tin-based alloys applied to electronic components are scarce in the literature. In general, the studies on this topic are on commercially pure or slightly modified metals with applications in the biomedical and pharmaceutical fields. Milheiro and coauthors[16] and Elshahawy et al.[17] reported that Sn does not exhibit toxicity, while metals such as Zn, Cu, and Ni are toxic at very low concentrations such as 10 ppm.

Much of the knowledge about solder alloys pertains to the impacts of their constituent elements. For instance, in a study by Ku and colleagues,[18] they assessed the toxicity, public health effects, raw material availability, and environmental effects of Pb and six alternative metals (Ag, Sb, Cu, Sn, In, and Bi). Pb was found to be the most toxic, followed by Ag and Sb, while Sn and Cu were the least toxic. Based on this, researchers suggest that SAC alloys, for example, exhibit lower cytotoxicity compared to traditional Sn−Pb. However, further research is needed to comprehensively evaluate alloy toxicity, considering the microstructure impact and enabling the best balance of properties to be attained.[18]

Researchers have employed various biocompatibility assessment methods to evaluate the cytotoxicity of Cu-, Ag-, and Cr-based solder alloys.[19−21] Most of these are tailored for use in specialized medical and orthodontic applications. These methods include cell viability assays, cell morphology analysis, and the evaluation of inflammatory responses. Results have demonstrated the importance of choosing solder alloys with minimal adverse effects on living cells. Under such a context, it is important to highlight the absence of research on cell viability concerning Sn-based lead-free alternative alloys and the influence of microstructures on cellular responses.

In addition to understanding the impacts of Zn on the solidification of the Sn−Ni alloy, we also assess its effect on cell

https://doi.org/10.1021/acsomega.3c06305
ACS Omega 2024, 9, 8829−8845

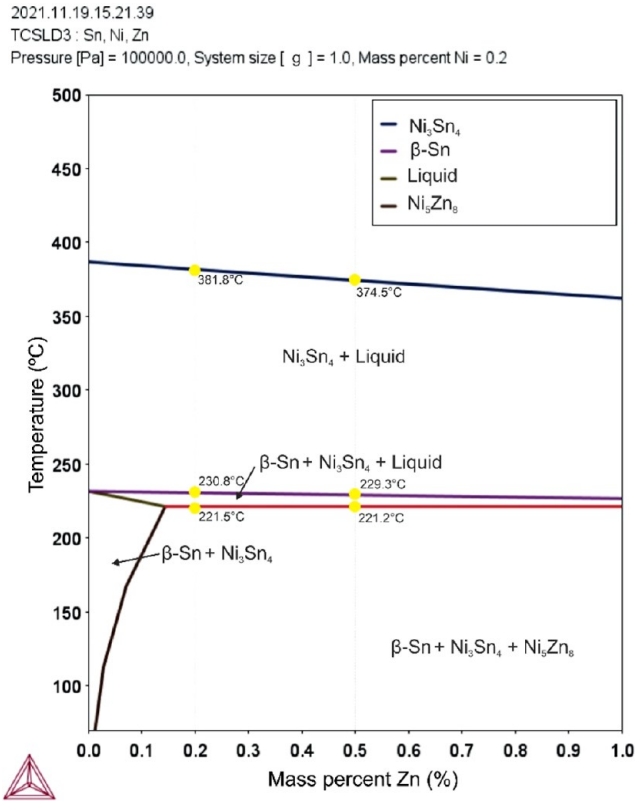

Figure 3. Sn-0.2 wt % Ni-*x*Zn isopleth computed by the Thermo-Calc software (TCSLD3 database).

viability for different Zn contents, various microstructures, and different incubation times.

This study seeks to investigate how the insertion of zinc (0.2% and 0.5 wt %) impacts the directionally solidified (DS) eutectic Sn-0.2 wt % Ni alloy, regarding the thermal parameters of solidification, as-cast microstructures, phase transformation, segregation, and cytotoxicity. In this last analysis, binary Sn−Pb and Pb−Sn alloy samples were produced and examined for comparison.

2. RESULTS AND DISCUSSION

2.1. Cooling Curves and Thermodynamics. The experimental thermal data (temperature × time) obtained during the directional solidification of Sn−Ni(-Zn) alloys are shown in Figure 1. Each line symbol in the records corresponds to a thermocouple positioned along the length of the casting, as outlined in the experimental procedure (Section 4). It is observed that thermocouples closest to the metal/mold plate interface exhibit a more pronounced slope in the temperature cooling curves over time during solidification. Conversely, for other thermocouples, there is a gradual decrease in these slopes. This different behavior of the cooling curves arises from the formation and evolution of the solidified layer as the thermal efficiency is higher at the onset of solidification (in the initially formed solidified layers). As solidification progresses, this efficiency diminishes due to increased thermal resistances associated with the growing thickness of the solidified layers, resulting in the observed inflection of the curves. Across all studied alloys, the cooling curves demonstrate stable cooling paths without any evident reheating attributed to shrinkage or inadequate adhesion of the metal to the substrate.

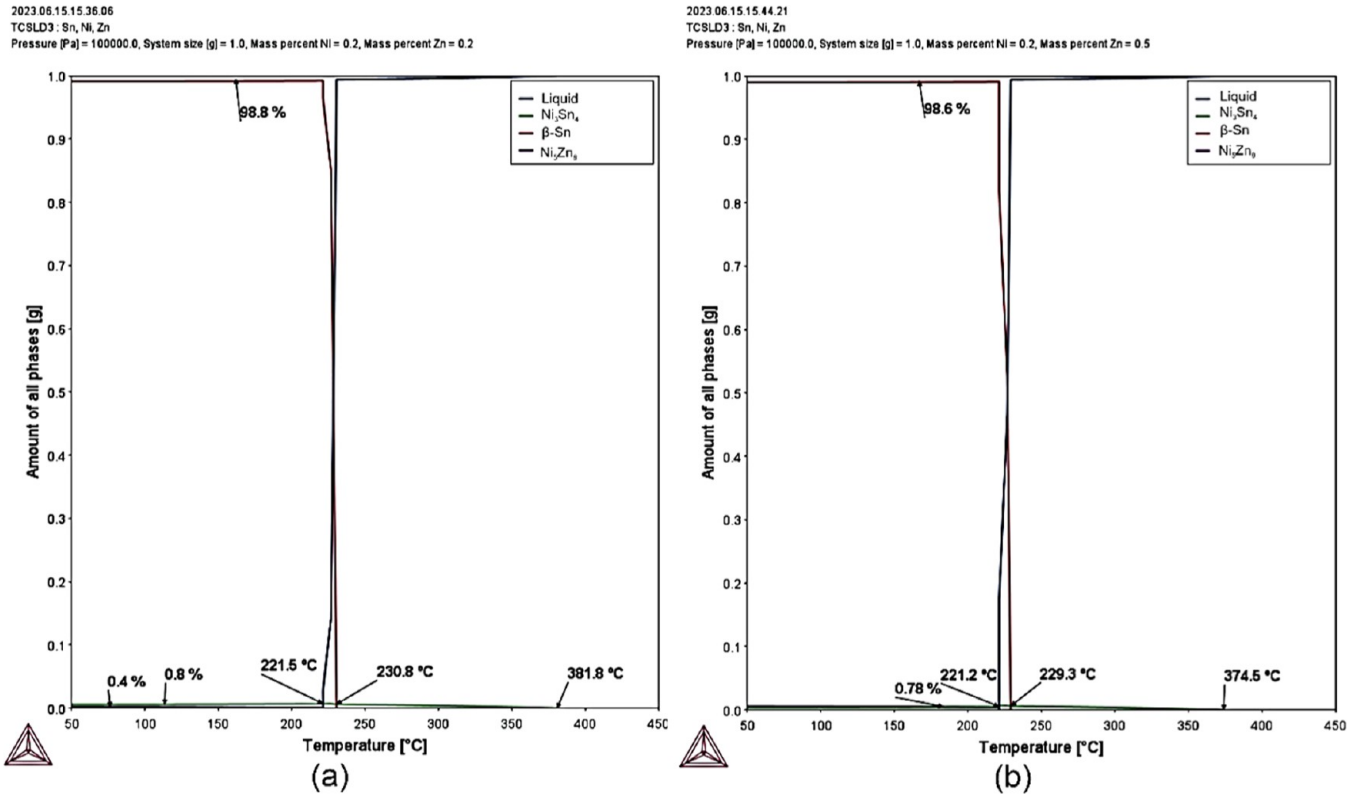

Figure 4. Equilibrium phase fractions versus temperature according to the CALPHAD method for: (a) Sn-0.2 wt % Ni-0.2 wt % Zn and (b) Sn-0.2 wt % Ni-0.5 wt % Zn solder alloys.

https://doi.org/10.1021/acsomega.3c06305
ACS Omega 2024, 9, 8829−8845

Table 1. Transformation Temperatures, Reactions and Phases for Sn-0.2 wt % Ni-0.2 wt % Zn and Sn-0.2 wt % Ni-0.5 wt % Zn Alloys, Predicted in Thermo-Calc Software

			temperature (°C)	
transformation	reaction	phases	Sn-0.2 wt % Ni-0.2 wt % Zn	Sn-0.2 wt % Ni-0.5 wt % Zn
liquidus Ni_3Sn_4–Nucleation	$L \rightarrow L + Ni_3Sn_4$	Ni_3Sn_4	381.8	374.5
β-Sn-nucleation	$L + Ni_3Sn_4 \rightarrow L + Ni_3Sn_4 + \beta$-Sn	$Ni_3Sn_4 + \beta$-Sn	230.8	229.3
ternary eutectic	$(L) + Ni_3Sn_4 + \beta$-Sn $\rightarrow$ $(Ni_5Zn_8 + Ni_3Sn_4 + \beta$-Sn)	$Ni_3Sn_4 + \beta$-Sn + $(Ni_5Zn_8 + Ni_3Sn_4 + \beta$-Sn	221.5	221.2

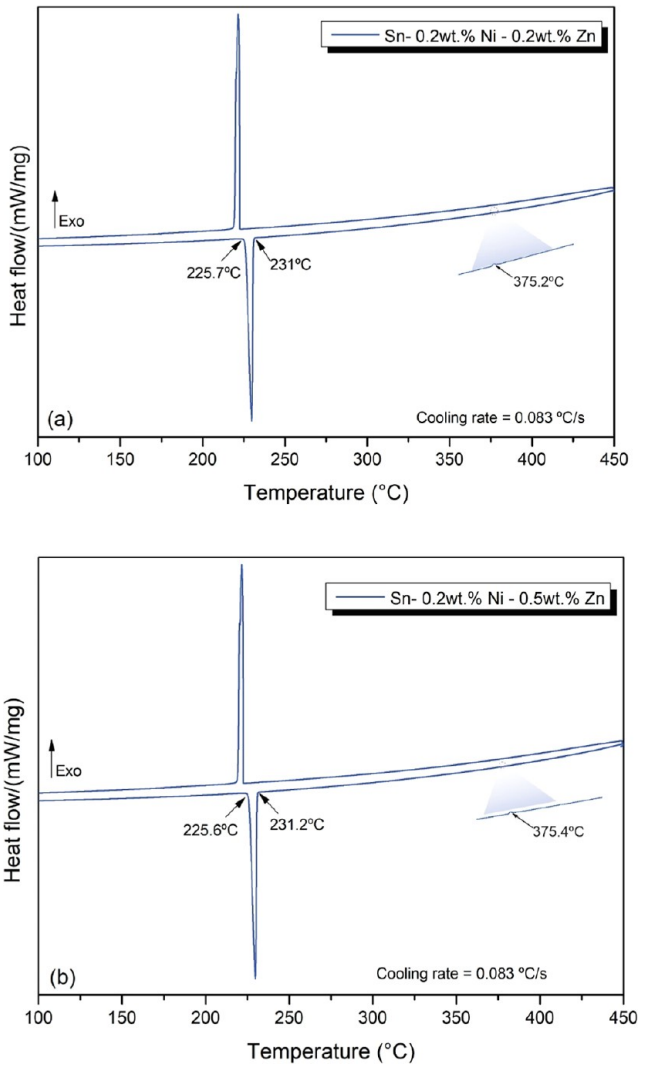

Figure 5. DSC for the (a) Sn-0.2 wt % Ni-0.2 wt % Zn and (b) Sn-0.2 wt % Ni-0.5 wt % Zn solder alloys.

Examining thermal profiles (temperature vs time data) enabled the assessment of crucial thermal solidification parameters, including cooling rate ($\dot{T}_L$) and velocity of the *liquidus* isotherm's movement (V_L). Figure 2 depicts the functions establishing correlations among V_L, $\dot{T}_L$, and the precise thermocouple positions for the Sn–Ni–Zn alloys. Taking into account the Sn–Ni–Zn alloys, the range of variation of the thermal parameters also showed a similar behavior when comparing both alloys, with the Sn-0.2 wt % Ni-0.5 wt % Zn solder alloy showing slightly higher V_L and $\dot{T}_L$ values. Compared to the binary Sn–Ni solder,[5] the addition of Zn promoted an increase in V_L, but without significantly affecting the cooling rate. The similarity of the thermal profiles of related sections in all of the alloys under investigation suggests that the temperature shifts during directional solidification were somewhat influenced by the increased Zn concentration.

Figure 3 presents the Sn-0.2 wt % Ni-*x*Zn isopleth, where the fixed composition of Ni is maintained at 0.2 wt % with variation in the Zn content (see dashed vertical lines). Table 1 presents a summary of the reactions, transformation temperatures, phases, and microstructures computed for the studied Sn–Ni–Zn alloys.

The microstructures of the Sn–Ni–Zn alloys are predicted to be formed by the following phases and their respective crystalline structures: β-Sn (body-centered tetragonal) and Ni_3Sn_4 (monoclinic).[11] The crystal structure of the Ni_5Zn_8 intermetallics was not reported in the literature, however, according to the Thermo-Calc software and based on the Hume–Rothery correspondence rule,[22] the intermetallic compounds Ni_5Zn_8 and Cu_5Zn_8 have the same crystalline structure. Therefore, the Cu_5Zn_8 compound of the γ phase has a complex cubic structure with 52 atoms per unit cell (Pearson symbol cI52) and lattice parameter of 8.86 Å.[23,24]

In Figure 4, the progression of phase solid fractions vs temperature is depicted for the Sn-0.2 wt % Ni-0.2 wt % Zn and Sn-0.2 wt % Ni-0.5 wt % Zn alloys under equilibrium thermodynamic conditions, as computed by the Thermo-Calc software. Considering the Sn-0.2 wt % Ni-0.2 wt % Zn alloy, it can be seen that the Ni_3Sn_4 primary phase nucleates at 381.8 °C. The remaining liquid continues cooling until it reaches 230.8 °C, where nucleation of the β-Sn phase occurs. Soon afterward, at 221.5 °C, all the remaining liquid transforms into the ternary eutectic: β-Sn + Ni_3Sn_4 + Ni_5Zn_8. The predicted solid fractions correspond to 98.8, 0.8, and 0.4% for the β-Sn, Ni_3Sn_4, and Ni_5Zn_8 phases, respectively.

The increase in Zn content did not produce significant variations in the solid fractions of the phases in the Sn-0.2 wt % Ni-0.5 wt % Zn alloy, except for the nucleation temperature of the Ni_3Sn_4 primary phase, which was reduced to 374 and 5 °C and a solid fraction of this phase corresponding to 0.78%. At 229.3 °C, the nucleation of the β-Sn phase occurs, followed by the transformation of all the remaining liquid into the ternary eutectic, β-Sn + Ni_3Sn_4 + Ni_5Zn_8 at 221.2 °C. The predicted solid fractions are 98.6, 0.78, and 0.62% for the β-Sn, Ni_3Sn_4, and Ni_5Zn_8 phases, respectively. As expected, the increase in Zn content promotes a slight increase in the solid fraction for Ni_5Zn_8 phase due to the preferential Ni–Zn reaction, whereas the β-Sn phase does not show any alteration.

The findings of phase change temperatures for each alloy under study were verified by thermal analysis utilizing the differential scanning calorimetry (DSC) technique while accounting for the cooling curves. Even with the low cooling rate (0.083 °C/s) utilized for heating and cooling in the DSC, there are some differences in the transition temperatures

https://doi.org/10.1021/acsomega.3c06305
ACS Omega 2024, 9, 8829–8845

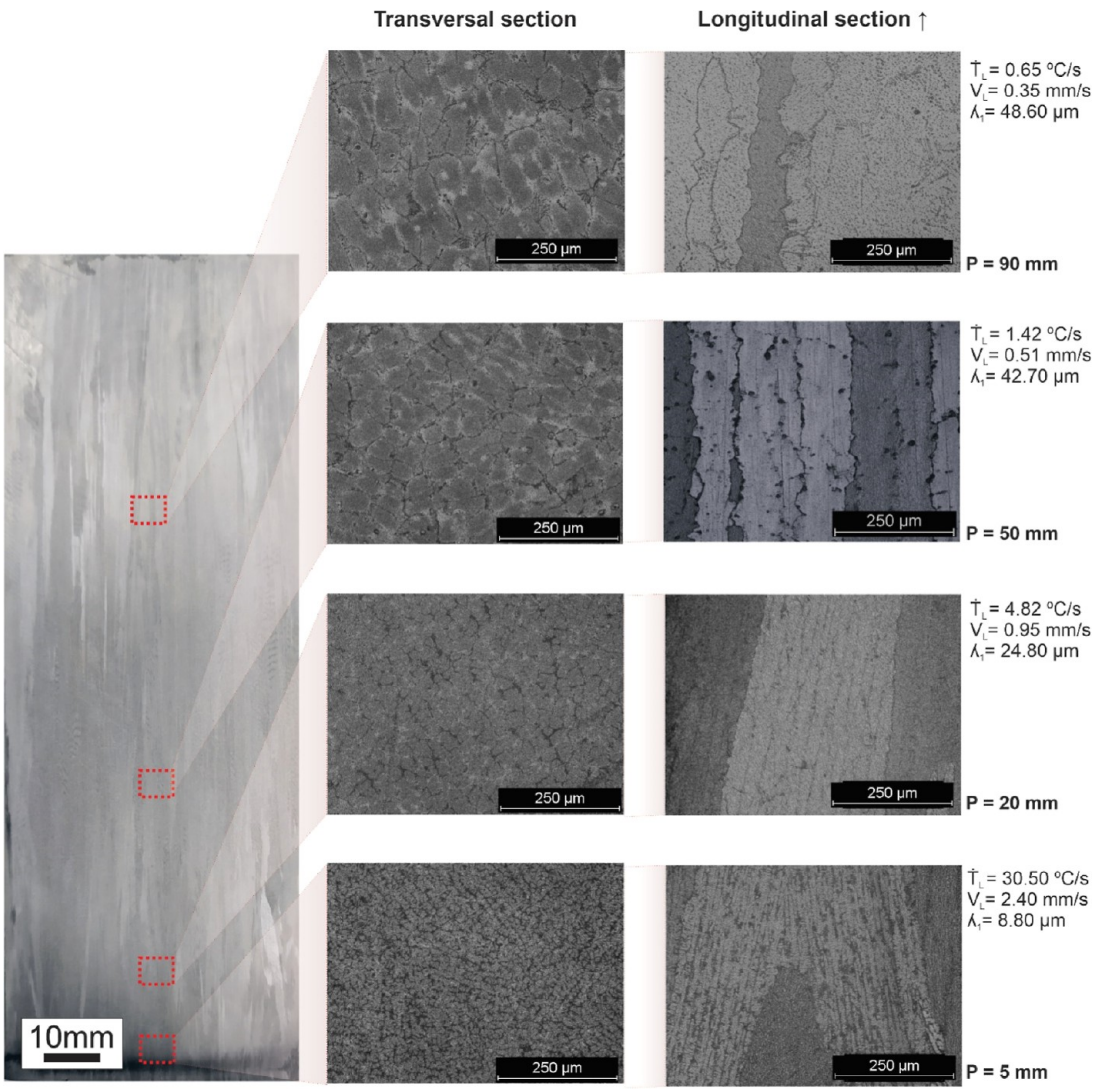

Figure 6. Macrostructure (highlighting some positions from the metal/mold plate interface) and typical as-cast microstructures along the length of the Sn-0.2 wt % Ni-0.2 wt % Zn alloy casting and their corresponding thermal parameters (cooling rate-$\dot{T}_L$ and growth rate-V_L) and primary dendritic arm spacings values.

compared to the equilibrium diagram produced by the Thermo-Calc. Furthermore, the endothermic and exothermic peak positions are not entirely symmetrical because subcooling of the particles during the solidification process may cause them to shift.[25]

Figure 5 shows the differential scanning calorimetry results of the Sn−Ni−Zn alloys. The endothermic curves displayed the temperatures of 225.7 and 231, and 225.6 and 231.2 °C, for the Sn-0.2 wt % Ni-0.2 wt % Zn and Sn-0.2 wt % Ni-0.5 wt % Zn solder alloys, respectively. It was observed that there was no significant variation in the heat flux values for the phase transformation temperatures of 375.2 and 375.4 °C of the Zn-modified alloys. In order to visualize the peaks associated with these temperatures, a zoomed-in clipping of the region was inserted into the graph. In general, the alloys of the Sn−Ni−Zn system presented similar results in relation to the transformation temperatures predicted by the Thermo-Calc software, with a slight difference only for the Sn-0.2 wt % Ni-0.2 wt % Zn alloy, in which a transformation temperature (*liquidus*) of 375.2 °C was obtained instead of the 381.7 °C given by the simulation.

2.2. Microstructural Scaling Relationships. The macrostructures and a few representative as-soldered microstructures (longitudinal and transverse sections) that were seen at various points throughout the Sn−Ni−Zn casting length are depicted in Figures 6 and 7. In addition, the primary dendritic arm spacing (λ_1) associated with each point from the metal/mold bottom base contact was entered along with the values of thermal parameters like growth rate (V_L) and cooling rate ($\dot{T}_L$). Optical microscopy was used to obtain all microstructures. It can be seen that the Sn−Ni−Zn alloys exhibited columnar growth with grains aligned parallel to the direction of heat extraction, indicating the directionality of the solidification process integrally in the castings.

Both alloys showed dendritic morphologies along their length, without occurrence of cellular/dendritic transition, contrary to what was reported by Xavier et al.[5] for the DS Sn-0.2 wt % Ni eutectic alloy out of equilibrium, where high-velocity cells developed in the initial positions of the ingot for high cooling rates. In general, the formed microstructures in Sn−Ni−Zn alloys are composed of a matrix rich in Sn (Sn-β phase) surrounded by a eutectic mixture composed of Ni_3Sn_4, NiSn,

https://doi.org/10.1021/acsomega.3c06305
ACS Omega 2024, 9, 8829−8845

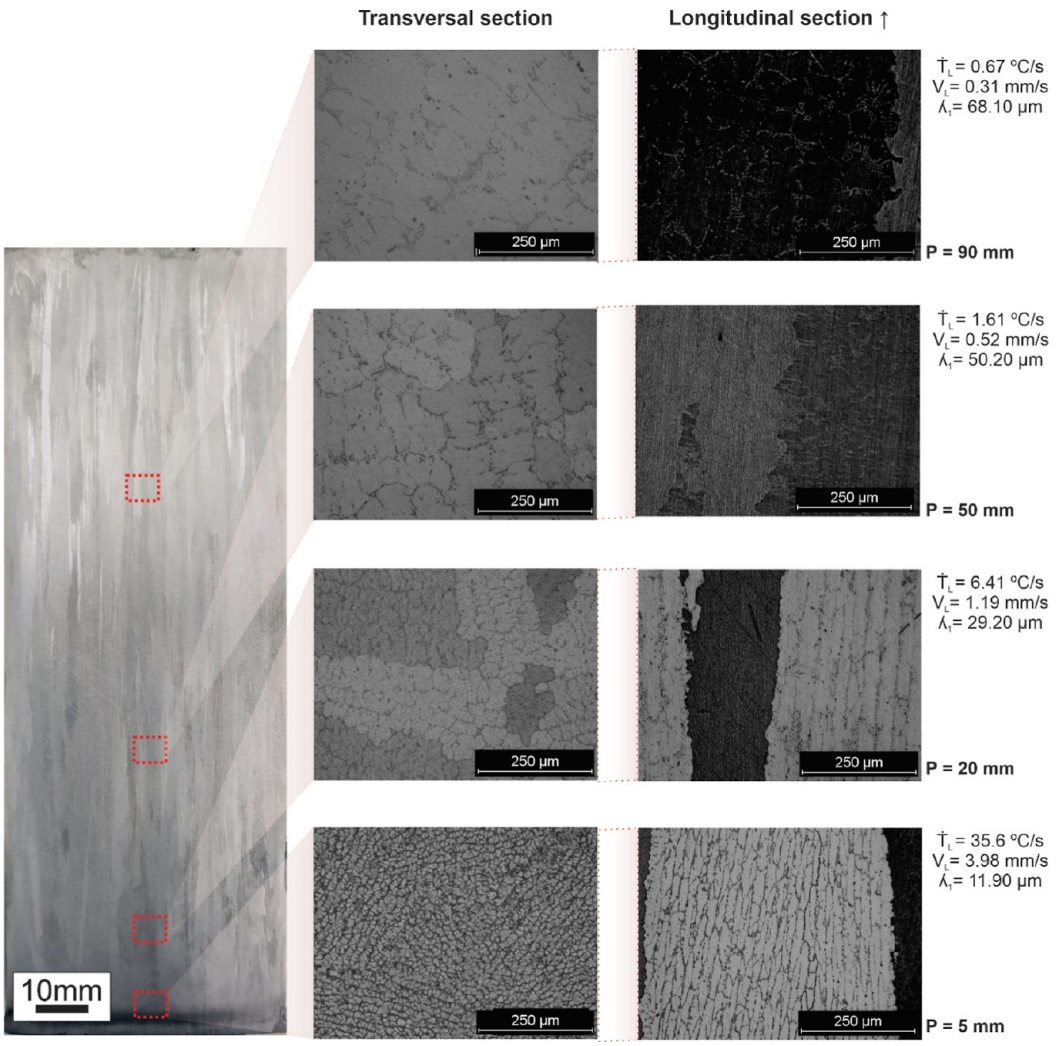

Figure 7. Macrostructure (highlighting positions from the metal/mold plate interface) and typical as-cast microstructures along the length of the Sn-0.2 wt % Ni-0.5 wt % Zn alloy casting and their corresponding thermal parameters (cooling rate-$\dot{T}_L$ and growth rate-V_L) and primary dendritic arm spacing values.

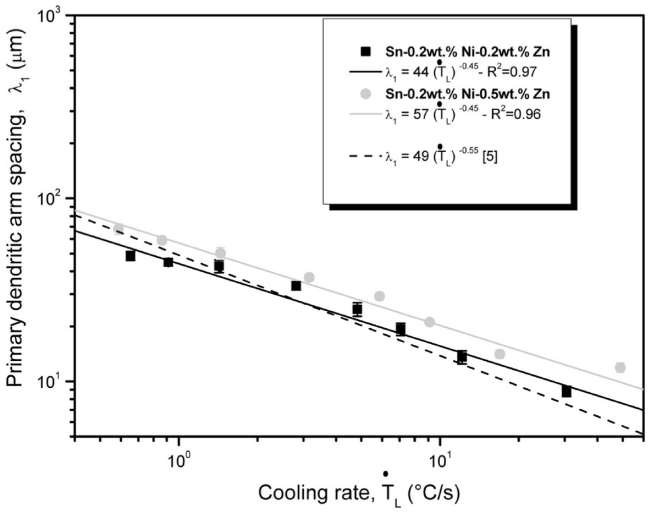

Figure 8. Primary dendritic arm spacing (λ_1) as a function of the cooling rate ($\dot{T}_L$) for the Sn−Ni−Zn solder alloys.

and Sn-β phases, in addition to a probable formation of $(Cu,Ni)_6Sn_5$ due to the diffusion from the Cu plate substrate. The presence of the NiSn intermetallics in the microstructure of the Sn−Ni−Zn alloys is explained by the fact that the directional solidification process occurs out of equilibrium, unlike what was observed for the simulations in the Thermo-calc software, which occur in thermodynamic equilibrium. As reported by Xavier et al.,[26] the dissolution of Cu from the substrate provided the formation of the $(Cu,Ni)_6Sn_5$ phase. However, Belyakov and Gourlay[7] reported that Ni from the dissolution of ENIG substrate (electrolytic nickel immersion gold) with Sn-x % Ni alloys (x = 0.07; 0.2; 0.45; in weight %) promotes the formation of the Ni_3Sn_4 phase through interfacial reactions.

The Sn-0.2 wt % Ni-0.2 wt % Zn alloy showed high cooling rates, reaching a value of 30.50 °C/s for the 5 mm position from the bottom plate, reducing to 0.65 °C/s for the 90 mm from the metal/mold plate interface, with growth rates varying between 2.40 and 0.35 mm/s. Primary dendritic spacing values (λ_1) ranged from 8.80 to 48.60 μm for positions 5 and 90 mm, respectively. In the case of the Sn-0.2 wt % Ni-0.5 wt % Zn alloy, the λ_1 values varied between 11.90 and 68.10 μm. Taking into account the thermal parameters, the Sn-0.2 wt % Ni-0.5 wt % Zn alloy exhibited cooling rate values between 48.90 and 0.60 °C/s for positions 5 and 90 mm from the metal/mold plate interface,

https://doi.org/10.1021/acsomega.3c06305
ACS Omega 2024, 9, 8829−8845

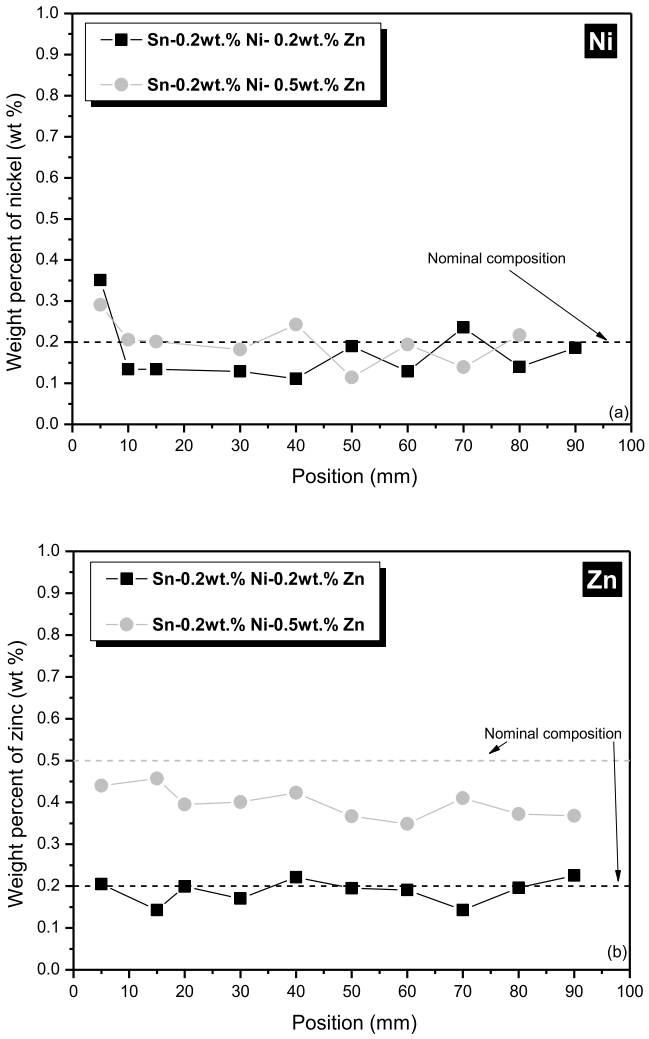

Figure 9. Experimental XRF macrosegregation profiles of (a) nickel and (b) zinc along the length of the Sn-0.2 wt % Ni-0.2 wt % Zn and Sn-0.2 wt % Ni-0.5 wt % Zn solder alloys. *P* is the position from the metal−mold plate interface.

with the growth rate between 3.60 and 0.30 mm/s for the same positions, respectively.

In general, Zn collaborated in increasing the values of the thermal variables ($\dot{T}$ and V), when compared with the values found for the binary Sn-0.2 wt % Ni alloy. The occurrence of high-velocity cells for $\dot{T}$ values greater than 5.5 °C/s was reported in Xavier et al.[26] for the DS Sn-0.2 wt % Ni alloy in a copper mold, followed by a reverse transition from cells to dendrites with decreasing cooling rate. On the other hand, for both Sn−Ni−Zn alloys examined, cooling rate values greater than 5.5 °C/s prevailed along the castings up to approximately 20 mm from the metal/mold plate interface without the growth of cells.

Extracted from the primary dendritic spacing (λ_1) correlations as a function of the cooling rate ($\dot{T}$) along the Sn-0.2 wt % Ni-0.2 wt % Zn and Sn-0.2 wt % Ni-0.5 wt % Zn alloy castings, Figure 8 displays the experimental equations reflecting microstructural growth. To assess the impact of the Zn content, the experimental expressions published by Xavier et al.[5] were also incorporated into the plots. The 40 measurements—mean microstructural spacing and corresponding mean variances—are shown as points on the graphs. The correlation coefficient between the linear relationship adjustments and the microstructural spacing values is represented by R^2.

The additions of Zn promoted a subtle growth in the microstructural scale of the Sn−Ni−Zn alloys, as can be seen in Figure 8. Considering the Zn additions examined here, it is noted that the increase in Zn content did not cause a significant effect on the scale of the dendritic arrangement, being characterized by the experimental expressions, $\lambda_1 = 44(\dot{T}_L)^{-0.45}$ and $\lambda_1 = 57(\dot{T}_L)^{-0.45}$ for the Sn-0.2 wt % Ni-0.2 wt % Zn and Sn-0.2 wt % Ni-0.5 wt % Zn solder alloys. The experimental exponents used for the Sn−Ni−Zn alloys are similar to those reported (−0.5 and −0.55) to describe the evolution of λ_1 as a function of $\dot{T}$ for other tin-based alloys such as Sn−Ag−Zn[27] and Sn−Ni.[5]

2.3. Phases Formed, Segregation, and Cytotoxicity.

The experimental profiles of zinc (Zn) and nickel (Ni) found by X-ray fluorescence (XRF) analysis are displayed in Figure 9 and correspond to certain locations along the Sn−Ni−Zn alloy castings. With acceptable deviations, the profiles validate the chemical composition of the studied alloys.

Ni showed inverse type macrosegregation profiles for both alloys, starting with levels higher than the nominal and decaying in the farthest positions from the metal/mold plate interface. Zn showed a slightly inverse macrosegregation behavior only in the Sn-0.2 wt % Ni-0.5 wt % Zn alloy, while for the Sn-0.2 wt % Ni-0.2 wt % Zn alloy, the Zn content remained around the nominal composition.

Figure 10 shows the X-ray diffractograms referring to the Sn−Ni−Zn solder alloys in three different positions and their respective cooling rates. The β-Sn, NiSn, and Ni_3Sn_4 phases have been detected for both alloys. The Ni_5Zn_8 intermetallics was not identified in the diffractograms despite being predicted in the Sn-0.2 wt % Ni-xZn isopleth as a very low fraction phase. The NiSn phase was identified in the X-ray diffraction (XRD) analyses, which was not predicted in the CALPHAD (Computer Coupling of Phase Diagrams and Thermochemistry) simulations, which are carried out under thermodynamic equilibrium conditions. In the context of the current findings, where solidification deviates from equilibrium, the emergence of novel phases becomes possible, as exemplified by the NiSn phase. The intensity of phase 2θ peaks did not follow any increasing or decreasing trend along the castings. The peaks associated with higher cooling rate for the Sn-0.2 wt % Ni-0.2 wt % Zn alloy showed greater intensity due to a higher volume fraction of the phases.

It is widely reported[28−30] that the Ni_3Sn_4 intermetallics is the only one formed that can be detected in the interfacial reaction layer between Sn-based alloys and Ni substrates. Using backscattered electron diffraction analysis (EBSD technique) on the $(Cu,Ni)_6Sn_5$ layer formed on the Sn-3.8 wt % Ag-0.7 wt % Cu alloy solidified against Ni substrate, Li et al.[31] reported that the existence of Ni in the $(Cu,Ni)_6Sn_5$ phase does not seem to affect the indexed diffraction patterns of the Cu_6Sn_5 phase, as they are based on the same crystal structures with small variations in the lattice constants. As previously reported, it seems that there was diffusion of copper in the alloys from the substrate in the directional solidification, but no Cu−Zn intermetallic compounds were detected in the diffraction patterns.

Surface dissolution of the substrate is a common phenomenon in the solder alloy/substrate interaction; upon contact with the molten solder alloy, the substrate alloying elements have the potential to alter the chemical composition of the solder alloy,

https://doi.org/10.1021/acsomega.3c06305
ACS Omega 2024, 9, 8829−8845

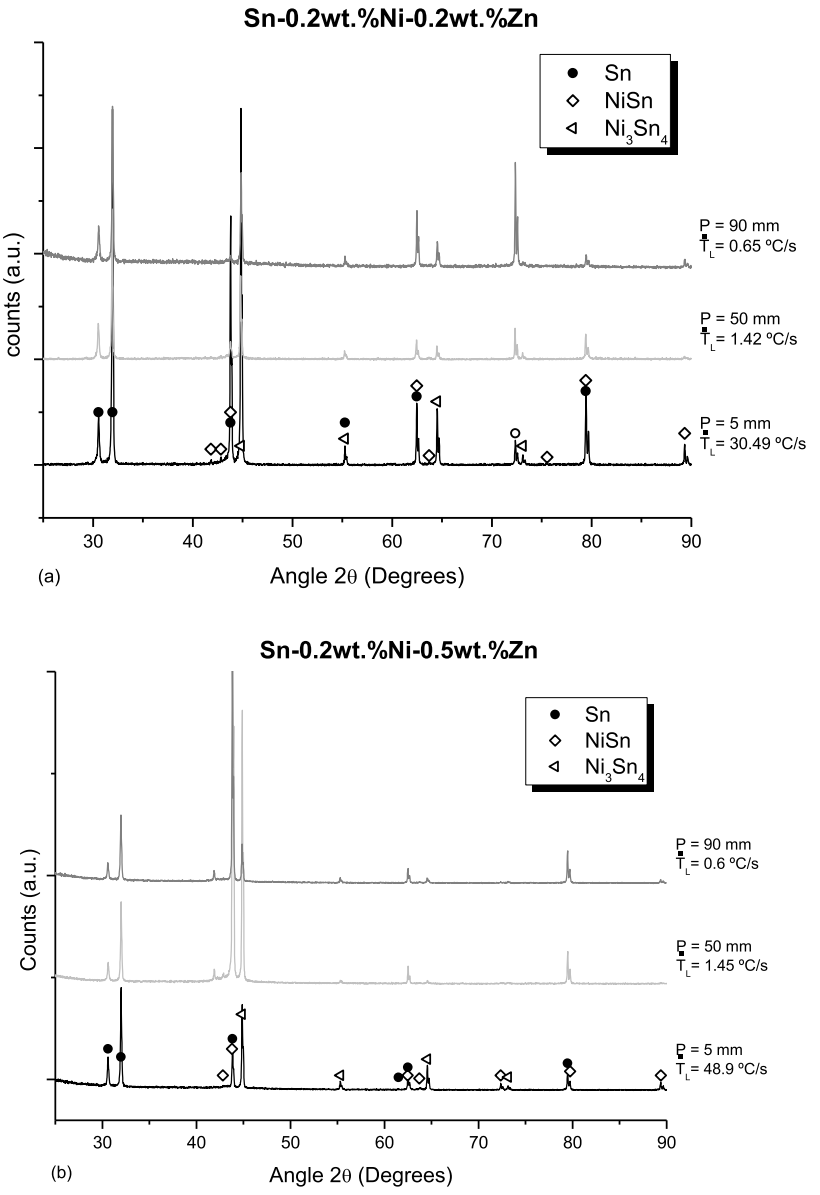

Figure 10. XRD patterns for samples of the (a) Sn-0.2 wt % Ni-0.2 wt % Zn and (b) Sn-0.2 wt % Ni-0.5 wt % Zn solder alloys. *P* is the position from the metal/mold plate interface.

resulting in the formation of unexpected phases. Other studies on solidification using copper as mold observed the dissolution of Cu and the presence of CuSn in regions farther from the mold surface.[5,26] Soares et al.[32] demonstrated the dissolution of Cu and Ni to the molten Sn−Cu alloy tested Sn−Cu/Cu and Sn−Cu/Ni couples during directional solidification.

As observed by Ng et al.,[33] as lead-free solder usage continues to grow, concerns have emerged regarding the dissolution of copper into lead-free alloys during the industrial process. The presence of copper in molten alloys can lead to sluggish soldering operations, primarily due to the formation of a denser copper−tin intermetallic (CuSn) compound. In contrast, with SnPb solders, the copper−tin intermetallic rises to the surface and can be easily removed. Another drawback is associated with the increase in the alloy's copper content, which raises the melting temperature. Consequently, the use of lead-free solder alloys may necessitate more frequent solder container maintenance due to their higher copper dissolution rates.

Although the NiSn compound does not usually appear as a stoichiometric compound on the Ni−Sn phase diagram, it is believed to be an extension of Ni_3Sn_2 from a lattice structure point of view.[34] Considering the joints soldered and their regions as the substrate, reaction layer (interfacial), and solder alloy, the metastable NiSn intermetallics is the first compound formed as a result of the soldering process. Nucleation of the NiSn phase can occur in the interfacial layer or in the diffusion zone. Given its comparably lower activation energy, the metastable NiSn compound exhibits a propensity for nucleation, a characteristic distinct from compounds like Ni_3Sn_4.[35]

Scanning electron microscopy (SEM) microstructure data for the Sn−Ni−Zn alloys are displayed in Figures 11 and 12, taking into account cooling rates and sections at 5 and 90 mm from the metal/mold plate interface. Before being observed in the microscope, immersion attacks were carried out for 2 min in order to emphasize the distribution and morphology of the intermetallics.

https://doi.org/10.1021/acsomega.3c06305
ACS Omega 2024, 9, 8829−8845

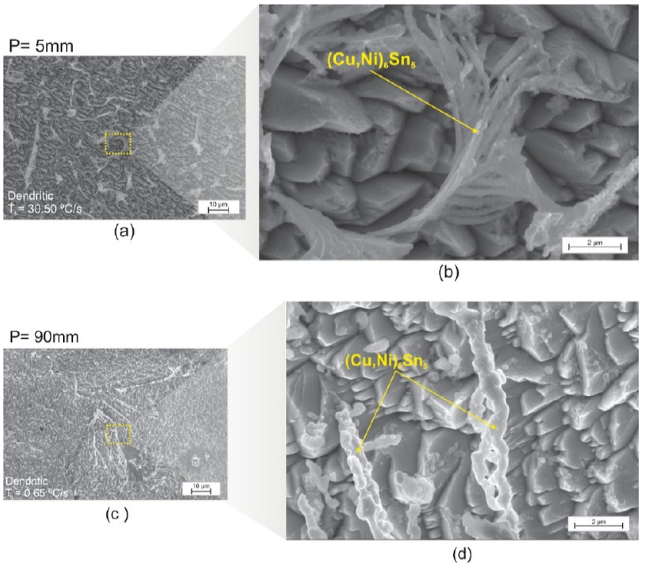

Figure 11. SEM as-cast microstructures of the Sn-0.2 wt % Ni-0.2 wt % Zn solder alloy highlighting the eutectic mixture and morphology of intermetallics for the (a,b) high and (c,d) low cooling rates.

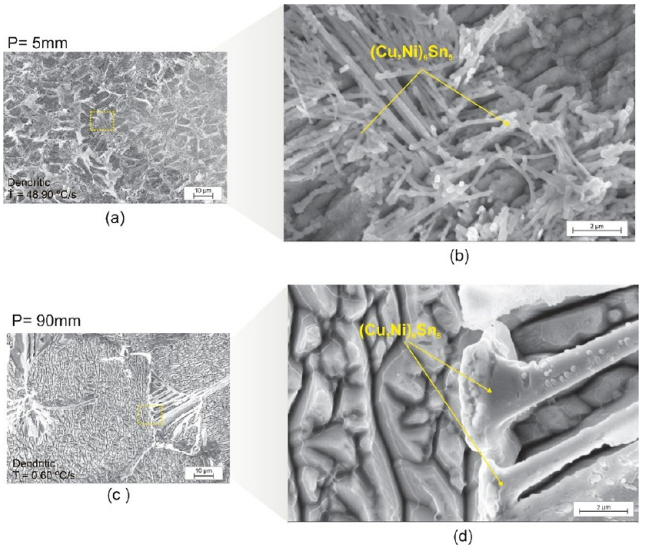

Figure 12. SEM as-cast microstructures of the Sn-0.2 wt % Ni-0.5 wt % Zn solder alloy highlighting the eutectic mixture and morphology of intermetallics for the (a, b) high and (c, d) low cooling rates.

It can be noted that in the microstructures related to the 5 mm position from the metal/mold plate interface, the Cu_6Sn_5 and $(Cu,Ni)_6Sn_5$intermetallic phases have fibrous morphologies and are arranged in feathering fiberlike structures in the interdendritic regions. Chemical analyses via SEM/EDS are presented in Figures 13 and 14, confirming this result. It is also possible to notice a reduction in the fraction of the intermetallic particles for both alloys at the 90 mm position from the metal/mold plate interface, in addition to the formation of thicker and elongated fibers. This result may be associated with the inverse-type macrosegregation of nickel, as previously reported. In the images obtained via SEM, it was not possible to identify the presence of intermetallics with a hexagonal crystal morphology as the Ni_3Sn_4 phase or of the NiSn intermetallics.

In order to quantitatively determine the chemical composition of the aforementioned intermetallic compounds, punctual EDS analyses were carried out for the Sn−Ni−Zn alloys, as shown in Figures 13 and 14. The selected samples correspond to the same positions (5 and 90 mm from the metal/mold plate interface) of the analyses for the SEM images, with high and low cooling rates.

The punctual EDS analyses indicated the presence of all the elements that make up the Sn−Ni−Zn alloys: Sn from the matrix, Zn and Ni resulting from intermetallics, and Cu from the substrate. Substrate dissolution can significantly alter the phases that form during solidification, particularly when the substrate is not the solder component.[36] Nogita[12] demonstrated that the high-temperature hexagonal phase (Cu_6Sn_5) can be stabilized when a concentration of around 9 at. % of Ni is present in the intermetallic particles to form the $(Cu,Ni)_6Sn_5$ phase. The incorporation of Ni makes the phase more thermodynamically stable at room temperature due to the delaying effect of Ni on the transformation of the hexagonal structure into a monoclinic one at 186 °C. The same authors observed rodlike structures for the $(Cu,Ni)_6Sn_5$ intermetallics, where the particles had an average content of 5.1 at. % of Ni.[12,37] However, Ni is not the only element to stabilize the Cu_6Sn_5 structure; Sb and Zn can influence the structure and stability of this intermetallics.[36,39] Nogita et al.[38] showed that Ni has the stabilizing effect of Cu_6Sn_5 in the range of 4.6−17.2 at. % of Ni at temperatures from −100 to 250 °C.

The results show that the fibers can be constituted of the $(Cu,Ni)_6Sn_5$ intermetallic, since there are fibers with a high concentration of Cu, with the exception of the fibers formed in 90 mm from the metal/mold plate interface for the Sn-0.2 wt % Ni-0.5 wt % Zn solder alloy, which presented lower Cu contents. All fibers formed had contents above 5 at. % of Ni. Therefore, this indicates that the developed fibers are constituted of the $(Cu,Ni)_6Sn_5$ intermetallics.

The MTT method was used to assess the cytotoxicity of the Sn−Ni−Zn alloys in order to comply with the regulations on the usage of Pb-free alloys[40] and to examine their cytotoxic behavior. Apart from the alloys mentioned earlier, reference samples such as the Sn-0.2 wt % Ni alloy and lead-containing alloys such as Pb-10 wt % Sn (high content) and Sn-20 wt % Pb (low content) alloys were also utilized for comparison. The latter is very toxic but is commonly used in microelectronic components. Verifying whether the microstructural scale affects the cytotoxic behavior of the alloys under investigation is another goal. For this, samples with high and low cooling rates associated with refined and coarse microstructures were selected, respectively, in this case, the positions of 5 and 90 mm from the metal/mold plate interface.

In view of the above, the analyzed samples first underwent an incubation period, being inserted into the culture medium (without cells) for three different times, 15 and 30 days, and calling them extracts. The samples were exposed to the culture medium for these times in order to verify if there would be the release of substances that could be identified as toxic when the extracts were inserted later along with the epithelial cell lineage, according to the experimental procedure already described in the section. Thus, after this incubation period of 15 and 30 days, cytotoxicity was evaluated at two different times of exposure of extracts to cells, 24 and 48 h (standard exposure times used in toxicology), being considered as satisfactory periods for the internalization and metabolization of the extracts of the studied alloys to the cells to occur.

Statistical calculations were employed to derive the percentages, averages, and standard deviations of cytotoxicity

https://doi.org/10.1021/acsomega.3c06305
ACS Omega 2024, 9, 8829−8845

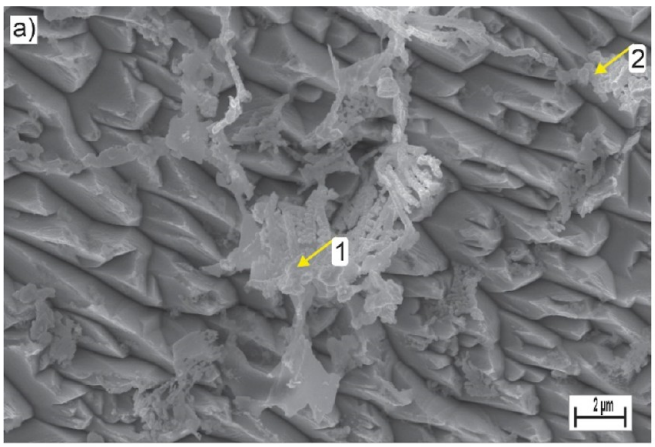

5mm	Sn-0.2wt%Ni-0.2wt%Zn							
	Sn		Ni		Zn		Cu	
Point	wt.%	at.%	wt.%	at.%	wt.%	at.%	wt.%	at.%
1	51.36	35.57	19.34	27.09	15.2	19.11	14.09	18.23
2	49.46	33.98	16.88	23.45	17.54	21.88	16.12	20.69

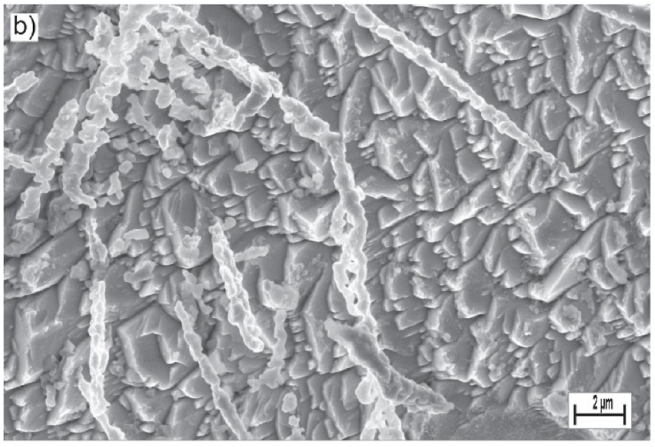

90mm	Sn-0.2wt%Ni-0.2wt%Zn							
	Sn		Ni		Zn		Cu	
Point	wt.%	at.%	wt.%	at.%	wt.%	at.%	wt.%	at.%
1	44.10	29.29	18.31	24.59	14.50	17.48	23.08	28.64
2	42.62	28.05	18.29	24.35	12.97	15.49	26.12	32.11
3	100	100	-	-	-	-	-	-

Figure 13. Compositional analysis of the phases by SEM/EDS for the Sn-0.2 wt % Ni-0.2 wt % Zn solder alloy, considering (a) 5 and (b) 90 mm positions from the metal/mold plate interface.

for each sample. It is noteworthy that these percentages are always relative to the 24 and 48 h bars of each alloy, with their respective positions compared to the bar containing negative control information (C−). This specific bar comprises DMEM (Dulbecco's Modified Eagle Medium—fetal bovine serum) in its pure form, devoid of contact with the samples, and exhibiting 88% cell viability, indicating approximately 88% of viable cells under the specified test conditions, as depicted in Figures 15 and 16.

Figure 15 shows the experimental cytotoxicity correlations for each alloy at the 5 and 90 mm positions over the 15 day incubation period, with the white bar representing the negative control (live cells) maintaining approximately 88% cell viability. In Figure 15a, it was observed that alloys containing lead (Pb) displayed elevated rates of cell death at 24 and 48 h. Cell viability for the Pb-10 wt % Sn alloy was 23 and 20%, while for the Sn-20 wt % Pb alloy, it was only 16 and 17%.

The levels of cell viability of the Sn-0.2 wt % Ni alloy was one of the lowest among the examined alloys. For the 24 and 48 h intervals, values of 19 and 14% were obtained, respectively. It is verified that the Zn additions promoted different cytotoxic responses for the Sn−Ni−Zn alloys. In the Sn-0.2 wt % Ni-0.2 wt % Zn alloy, in 24 and 48 h, cell viability values of 14 and 63% were found, respectively. The Sn-0.2 wt % Ni-0.5 wt % Zn alloy showed similar cytotoxic responses in both contact periods, around 35%. Considering the 90 mm position (Figure 15b), the alloys showed variations in cytotoxicity in relation to 5 mm. First, the Pb-containing alloys still maintained a highly toxic effect.

An increase in cell viability in the 24 h contact period for Sn−Ni−Zn has been noticed, but still with percentages below 50%. For the 48 h period, there was a reduction in cell viability for both Sn−Ni−Zn alloys, with emphasis on the Sn-0.2 wt % Ni-0.5 wt % Zn alloy, which showed only 5%. This fact may be associated with spontaneous cell death and not necessarily due to the influence of the sample.

Figure 16 shows cell viability data for the 5 and 90 mm positions with an incubation time of 30 days. It is noted that the Pb-containing alloys did not show significant variation in cytotoxicity, in relation to both the time of exposure with the cells (24 and 48 h) and the position (5 and 90 mm). Regarding the incubation period, there was a slight reduction in cell viability. This occurred mainly for the Sn-20 wt % Pb alloy, which exhibited cell viability levels of 12 and 10% for 24 and 48 h, respectively, considering the 90 mm samples.

Cells composed of extracts of Sn-0.2 wt % Ni alloys did not show significant changes in cell viability in relation to the incubation period, position, and exposure time, where high rates of cell death are still observed. Considering the Sn−Ni−Zn alloys, it is noticed that the cell viability improved in relation to the microstructural scale. For example, in the 24 h period, the cell viability of the Sn-0.2 wt % Ni-0.2 wt % Zn alloy went from 19 to 60%, from the 5 mm position to 90 mm, respectively, an increase of 3 times. Taking into account the 5 mm position and 48 h period for the Sn-0.2 wt % Ni-0.5 wt % Zn alloy, complete

https://doi.org/10.1021/acsomega.3c06305
ACS Omega 2024, 9, 8829−8845

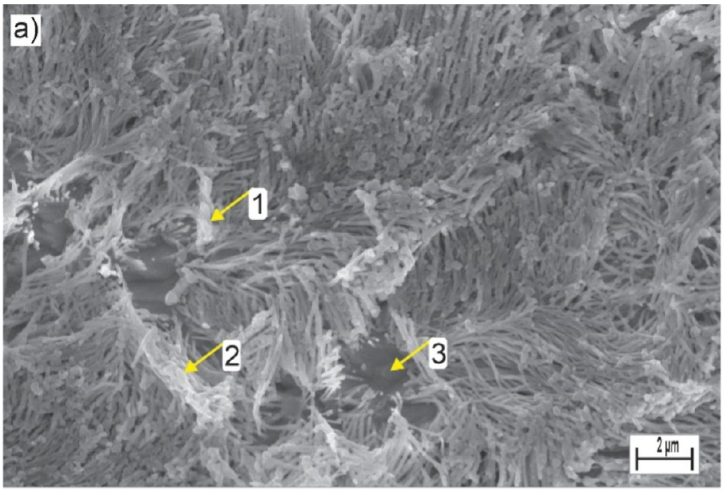

5mm	Sn-0.2wt%Ni-0.5wt%Zn							
	Sn		Ni		Zn		Cu	
Point	wt.%	at.%	wt.%	at.%	wt.%	at.%	wt.%	at.%
1	55.31	38.13	4.15	5.98	12.41	16.05	29.93	39.84
2	41.75	27.74	5.03	6.76	15.69	18.92	37.53	46.58
3	100	100	-	-	-	-	-	-

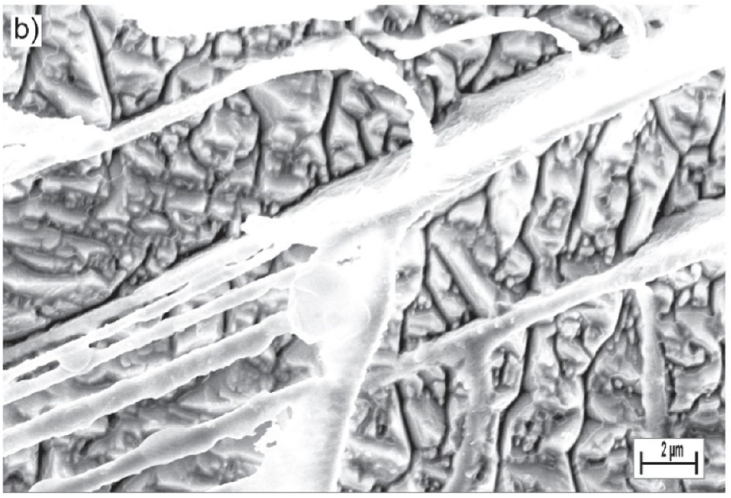

90mm	Sn-0.2wt%Ni-0.5wt%Zn							
	Sn		Ni		Zn		Cu	
Point	wt.%	at.%	wt.%	at.%	wt.%	at.%	wt.%	at.%
1	79.48	67.46	5.06	8.69	14.61	22.52	0.84	1.34
2	58.17	42.22	16.13	23.68	19.61	25.83	6.1	8.27
3	48.25	32.91	19.94	27.51	25.85	32	5.95	7.58
4	46.22	30.89	25.52	34.49	19	23.05	9.27	11.57

Figure 14. Compositional analysis of the phases by SEM/EDS for the Sn-0.2 wt % Ni-0.5 wt % Zn solder alloy, considering (a) 5 and (b) 90 mm positions from the metal/mold plate interface.

cell death was observed. Regarding the incubation period (from 15 to 30 days), the toxic character of the Sn−Ni−Zn alloys increased at the 5 mm position and generally remained at 90 mm, with the exception of the Sn-0.2 wt % Ni-0.2 wt % Zn alloy, which had its viability improved, reaching 60% within 24 h.

3. CONCLUSIONS

The following conclusions can be drawn from this experimental study:

- Zn caused a significant increase in the melting temperature of the Sn-0.2 wt % Ni alloys, from 231 to 375 °C for both additions (0.2 and 0.5);
- In the as-cast microstructures of the Sn−Ni−Zn alloys, a predominantly dendritic microstructure composed of a Sn-rich matrix (β-Sn) surrounded by a eutectic mixture with Ni_3Sn_4, NiSn, and Sn-β phases has been noted. Furthermore, there was an apparent indication of $(Cu, Ni)_6Sn_5$ formation, likely triggered by the transportation of Cu from the bottom plate, resulting in its dispersion within the bulk alloy;
- Zn did not affect the primary dendrite arm spacing of the Sn−Ni−Zn alloys when compared to the Sn-0.2 wt % Ni alloy. The increase in Zn content did not significantly influence the microstructural scale in Sn−Ni−Zn alloys;
- Microstructural scale did not affect the cytotoxic Sn−Ni−Zn alloy. However, the cytotoxic nature was influenced by the chemical composition and the period of incubation (15 and 30 days). Zn additions decreased toxicity while maintaining a moderate level of cytotoxicity.

4. EXPERIMENTAL PROCEDURE

The methodology adopted in the development of the study of eutectic Sn-0.2 wt % Ni alloys modified with small additions of zinc (Zn) (0.2% and 0.5 in weight %) and DS against a copper (Cu) mold-plate consisted of the following steps:

4.1. Simulations by CALPHAD. Thermodynamics calculations by the CALPHAD method using Thermo-calc software, version 2021a (TCSLD3 base), were performed, in order to obtain information such as *solidus*, *liquidus*, and eutectic transformation temperatures and isopleths of the Sn-0.2 wt % Ni-*x*Zn system, considering the variation in Zn content (0.2% and 0.5 in wt %). In addition, acquisitions of phase diagrams, phase mass fraction variation as a function of temperature, simulations of solidification paths, phase quantity, and compositions and solubility limit were made.

4.2. Preparation, Casting, and Directional Solidification. The Sn−Ni−Zn alloys were obtained from the

https://doi.org/10.1021/acsomega.3c06305
ACS Omega 2024, 9, 8829−8845

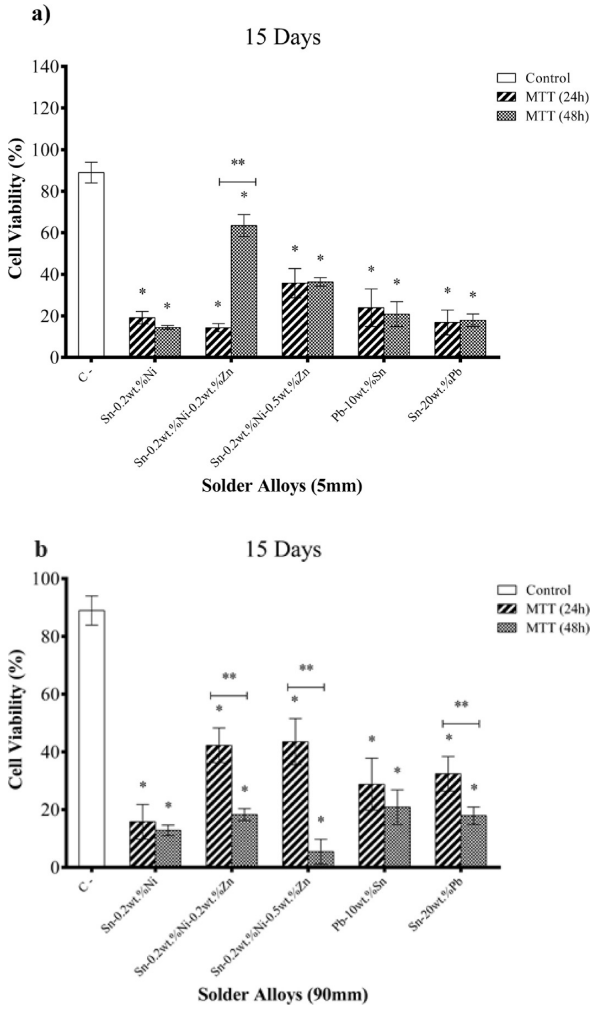

Figure 15. Cell viability (cytotoxicity effects) in mouse fibroblast cells (3T3) exposed to Sn−Ni−Zn, Sn−Ni, Sn−Pb, and Pb−Sn solder alloys (a) 5 and (b) 90 mm samples for 15 days, measured by MTT assays. DMEM culture medium was used as a negative control for cytotoxicity. Comparisons between groups were analyzed using ANOVA with Tukey's post-test.

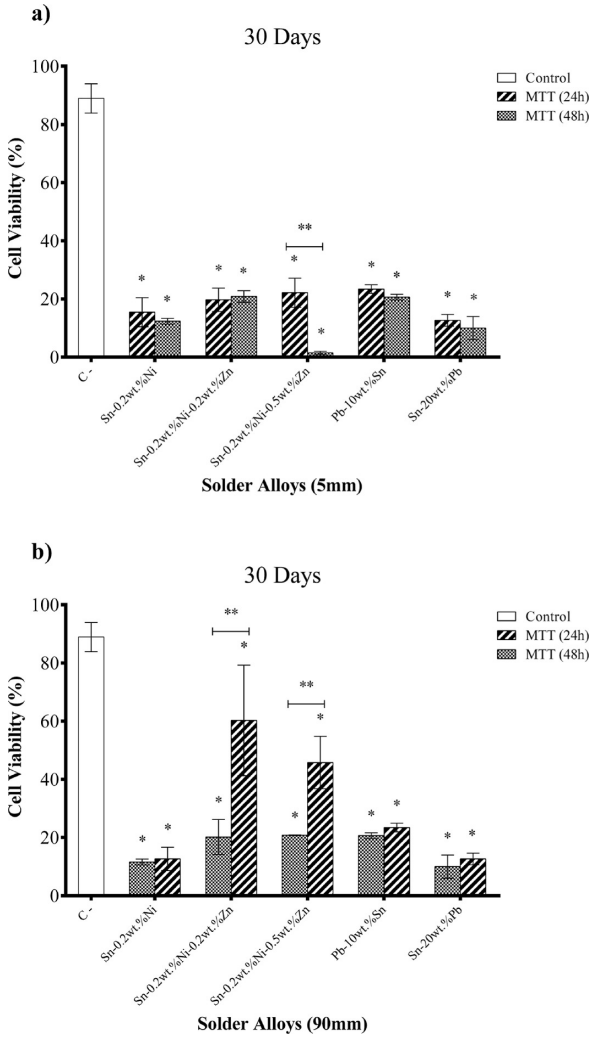

Figure 16. Cell viability (cytotoxicity effects) in mouse fibroblast cells (3T3) exposed to Sn−Ni−Zn, Sn−Ni, Sn−Pb, and Pb−Sn solder alloys (a) 5 and (b) 90 mm samples for 30 days, measured by MTT assays. DMEM culture medium was used as a negative control for cytotoxicity. Comparisons between groups were analyzed using ANOVA with Tukey's post-test.

commercially pure elements tin (Sn), nickel (Ni), and zinc (Zn). Table 2 presents the chemical composition of these metals.

Sn-0.2 wt % Ni-0.2 wt % Zn and Sn-0.2 wt % Ni-0.5 wt % Zn alloys were DS against the electrolytic Cu mold-plate (Figure 17).

The preparation of the alloys involved the following steps:

i Cutting and weighing (Sartorius, BP210S model) of metals (Sn, Ni, and Zn) considering the stoichiometric calculations performed for the chemical compositions;

ii Preparation of a silicon carbide crucible coated with a layer of refractory material (cement QF-180) to increase durability and avoid contamination of the alloys. The Sn pieces were first placed inside the crucible and placed in a Yuelon induction furnace (MF-35 model) with a working temperature between 300 and 400 °C. Afterward, Ni pieces were introduced when there was a remaining average time of 1 h. After this period, the crucible was removed and Zn was added to the liquid metal, and the solution was stirred with a steel rod coated with refractory material to ensure homogenization after approximately 10 min;

iii Fusion and homogenization of all components with subsequent pouring of liquid metal into the mold. Solidification occurs naturally in the mold and another amount of liquid metal is poured into a silicon carbide crucible (150 mm diameter × 175 mm height) with a thermocouple fixed inside, in order to monitor and extract the experimental transformation temperatures such as *liquidus* (T_L), eutectic (T_E), and *solidus* (T_S). A comparison of the experimental liquidus temperatures with those predicted by CALPHAD allowed confirming the alloy compositions;

iv The naturally solidified metal is then heated by activating the electrical resistances until the thermocouple closest to the metal/mold plate interface reaches the pouring temperature, corresponding to 10% of the eutectic and/or *liquidus* temperature of the examined alloy. Soon after, the furnace heating system was turned off, allowing the temperature to stabilize, and the cooling system (using water) was immediately activated, starting to cool the copper mold-plate (3 and 100 mm in thickness and

https://doi.org/10.1021/acsomega.3c06305
ACS Omega 2024, 9, 8829−8845

Table 2. Chemical Composition of Pure Metals Provided by the Manufacturer

	chemical composition (in wt %)							
metal	Sn	Cu	Ni	Zn	Sb	Cd	Pb	Fe
Sn	99.96	<0.001	<0.001	<0.001	0.03	0.02	0.025	0.003
Ni			99.96					0.0024
Zn	0.0001	0.0006		99.996		0.0003		0.0004

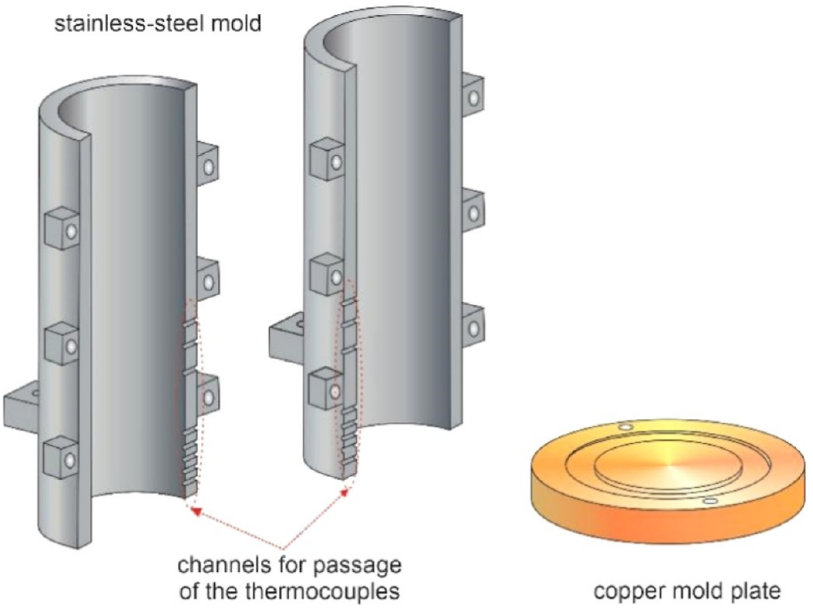

Figure 17. Stainless-steel mold and electrolytic Cu mold-plate.

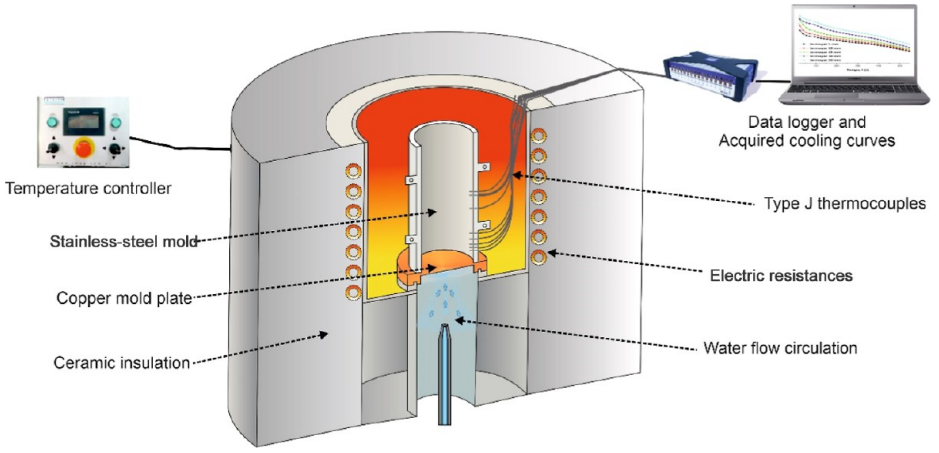

Figure 18. Representation of the directional solidification device.

diameter, respectively) mounted under the mold and consequently the liquid metal, allowing the onset of directional solidification;

v The thermal evolution inside the ingot mold was recorded by means of J-type thermocouples with 1.6 mm of diameter positioned along the ingot with the support of a data acquisition system (Keysight, Agilent 34901a model) and computer, as shown in Figure 18.

4.3. Solidification Thermal Variables. The solidification thermal parameters such as the growth rate of the *liquidus* isotherm (V) and cooling rate ($\dot{T}$) at each position along the examined castings were determined from the experimental cooling curves, displaying graphs of the variation of temperature (T) with time (t) during the directional solidification process.

Knowing the time and temperature data along each casting and the respective positions of the thermocouples, it is possible to perform an interpolation procedure in order to find the passage time of the liquidus isotherm (t) at each monitored point. Thus, an experimental graph correlating the position and time of the liquidus isotherm is drawn. Soon after, a curve is created that represents the displacement of this isotherm throughout the solidified ingot, and the data are mathematically adjusted by the computer program through the method of least-squares, generating a function $P(t) = a{\cdot}t^b$, being "a" and "b" constants. The derivative of these functions against time resulted in values for the growth rate (V). Moreover, the employed data

https://doi.org/10.1021/acsomega.3c06305
ACS Omega 2024, 9, 8829−8845

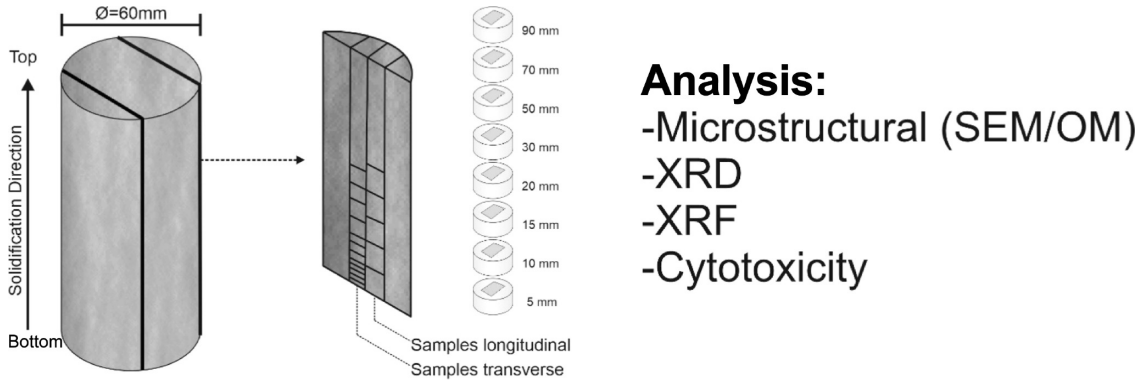

Figure 19. Schematic representation of removal of specimens from the Sn−Ni−Zn alloy castings in the longitudinal and transverse directions for microstructural, XRD, XRF, and cytotoxicity analysis.

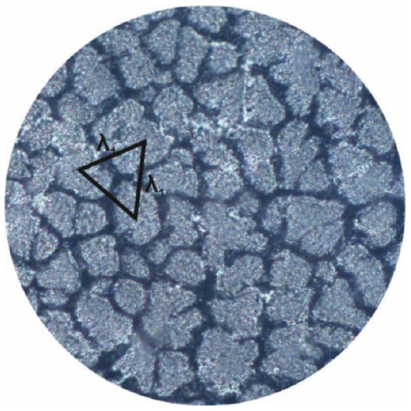

Figure 20. Schematic representations used for measurement procedures related to primary dendritic arm spacings (λ_1).

acquisition system permitted accurate determination of the slope of the experimental cooling curves (cooling rate $\dot{T} = dT/dt$) immediately after the passage of the *liquidus* isotherm by each thermocouple position along the length of the Sn−Ni−Zn solder alloys.

4.4. Characterization: Macrostructural and Microstructural. From the DS Sn−Ni−Zn solder alloys, longitudinal sectioning was carried out (parallel to the heat extraction direction) using a band saw (FM-500 model) to obtain the sample used in the macrostructural analysis and, subsequently, in the other part, transverse cuts were performed using a hacksaw to subsequent analyses, as shown in Figure 19 and in accordance with ASTM E3−11.[41]

In order to characterize the macrostructures, a longitudinal cut in each DS casting was made with subsequent grinding (120, 240, 320, 400, 600 grit SiC papers) followed by macroetching with the 100 mL of de H_2O, 2 mL of HCl and 5 g of $FeCl_3$ solution during 60 s. The macroetching was performed by immersion. Subsequently, the sample was washed in running water, dried with ethyl alcohol, and subsequently recorded using a camera/scanner.

Transverse and longitudinal samples (at 5, 10, 15, 20, 30, 40, 50, 60, 70, and 90 mm from the cooled bottom of the castings) were removed of each DS alloy casting for the metallographic procedure: (i) cold mounting with polyester resin; (ii) grinding using 120, 240, 320, 400, 600, 1200, and 2000 grit SiC papers; (iii) polishing (Teclago polisher, PVVD model) with a 1 μm alumina solution and water; iv. microetching with the 50 mL of de H_2O, 1 mL of HCl, and 5 g of $FeCl_3$ reagent during an interval between 3 and 5 s; (v) image acquisition via optical microscopy analyses using a Nikon instrument (Eclipse MA200 model). The as-cast microstructures were analyzed by an image processing

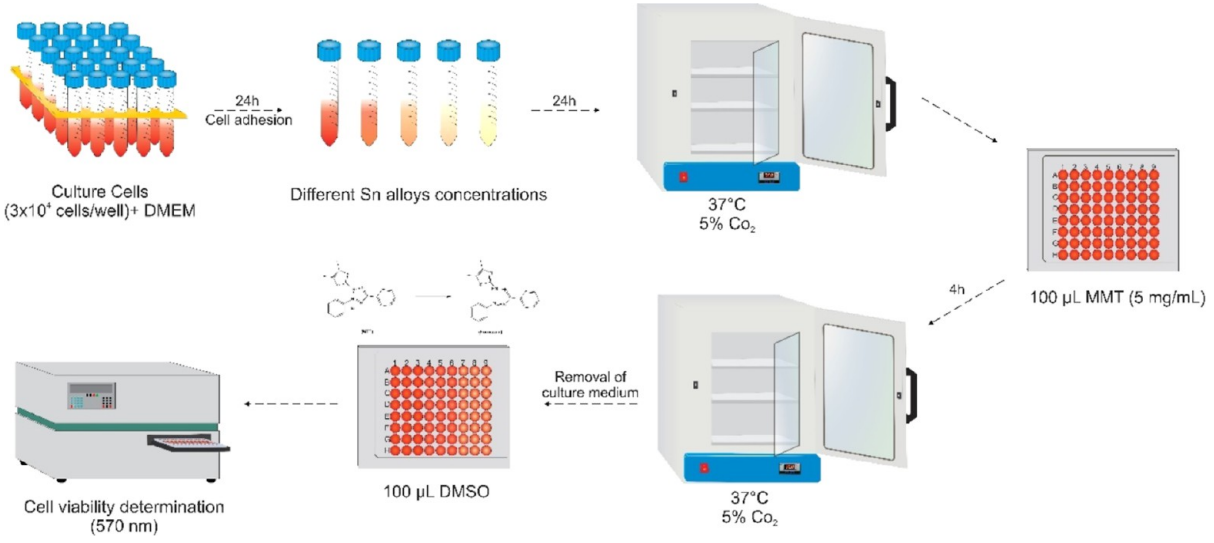

Figure 21. MTT assay protocol for cell viability and proliferation.

https://doi.org/10.1021/acsomega.3c06305
ACS Omega 2024, 9, 8829−8845

Figure 22. Schematic representation of the Alamar Blue cytotoxicity assay.

system, *ImageJ*. The generation of many samples allowed for the examination of a variety of dendritic configurations with varying length scales to investigate the effects of the cooling rate. Furthermore, this variety was generated to test the effects on the cytotoxicity levels.

With the microstructures revealed and registered, it was possible to measure the primary (λ_1) dendritic arm spacings. Thus, to measure λ_1, the cross section (which is perpendicular to the direction of heat extraction) was considered, as well as the neighborhood criterion, which considers the spacing value equal to the average distance between the geometric centers of the primary dendritic trunks in question, as indicated by the triangle method (Figure 20).[42] In order to obtain an average of values and a dispersion interval, 40 measurements were performed for each selected position.

In order to investigate in detail as-cast microstructures of solidification of the Sn−Ni−Zn alloys, analyses were carried out using SEM with field-emission gun (SEM-FEG), and a coupled energy-dispersive spectroscopy (EDS) detector at positions 5, 20, 50, and 90 mm from the metal/mold plate interface of the castings, which encompass the cooling rates along the DS castings. An immersion microetching using the 50 mL of de H_2O, 1 mL of HCl, and 5 g of $FeCl_3$ solution was carried out for 2 min in order to highlight the intermetallic particles in the as-cast microstructures.

In order to determinate macrosegregation profiles along the Sn−Ni−Zn castings, XRF technique was used to quantify the copper, nickel, and zinc contents in the transverse samples: 5, 10, 15, 20, 30, 40, 50, 60, 70, 80, and 90 mm from the metal/mold plate interface. The equipment used was a Shimadzu EDX-720 model. In order to identify the phases formed in the as-cast microstructures along the length of the DS castings, XRD tests were performed for specific positions in the DS castings (5, 10, 20, 50, and 90 mm from the metal/mold plate interface). Cross-sectional samples were used for this analysis. They were ground from 400 to 1200 mesh, having dimensions of 10 × 10 × 10 mm. The positions were selected based on the values of cooling rate (high, intermediate, and low).

XRD spectra were obtained using a Shimadzu XDR-700 diffractometer with a 2θ range from 20 to 90°, Cu Kα radiation, and a wavelength, λ, of 0.15406 nm and recorded at a scan speed of 2°/min.

4.5. Thermal Analysis−Differential Scanning Calorimetry. Thermal analyses were carried out in a differential scanning calorimeter on the DSC PerkinElmer equipment (8000/8500 model), where the samples were conditioned in an aluminum crucible, with a temperature ranging from 25 to 450 °C, a heating rate of 5 °C/min, and an atmosphere of nitrogen with a gas flow of 50 mL/min, using a mass of approximately 45 mg. Samples extracted from the ingots were machined to have dimensions of approximately 4 mm in length and 2 mm in thickness for the DSC. These samples were subjected to heating until complete melting, followed by cooling until complete solidification. The exothermic and endothermic curves generated during the phase transformations due to the release or absorption of energy are graphically represented, allowing the determination of the phase transformation temperatures.

4.6. Cytotoxicity Tests. With the aim of investigating the toxicity of the Sn−Ni−Zn alloys, cytotoxicity tests (cell viability)[43] were carried out using the Pb-10 wt % Sn and Sn-20 wt % Pb alloys as a standard for comparison. Furthermore, the effect of Zn content and microstructural scale on the cytotoxicity behavior of each DS casting has been evaluated. Cylindrical samples measuring 2 mm × 2 mm taken from the 5 and 90 mm positions from the metal/mold plate interface were used in the analyses.

Cytotoxicity was evaluated using a method based on measuring the activity of the mitochondrial dehydrogenase enzyme which, when active, is capable of metabolizing the MTT reagent—[3-(4,5-dimethylthiazol-2-yl)-2,5-bromide of diphenyltetrazolium] (a water-insoluble, yellow salt) into a colored compound called formazan (a water-insoluble, purplish-colored salt). The experimental procedure adopted is presented below:

4.7. Cell Viability by 3-(4,5-Dimethylthiazol-2-yl)-2,5-diphenyltetrazolium Bromide Assay. Cytotoxicity (cell viability) was determined in mouse fibroblast cells (3T3) using the MTT assay. Cells were grown under standard conditions in DMEM (Invitrogen, San Diego, CA, USA), supplemented with 10% fetal bovine serum at 37 °C in a humidified atmosphere with 5% CO_2, and collected after treatment with trypsin. Cells (1×10^5 cells per well) were seeded in the same medium and

https://doi.org/10.1021/acsomega.3c06305
ACS Omega 2024, 9, 8829−8845

cultured for 24 and 48 h in 96-well microplates to promote adhesion. Subsequently, the cells were individually incubated in triplicate so that their cytotoxicity could be evaluated with the different chemical compositions of the alloys under study, after which they were incubated at 37 °C for 24 and 48 h. Then, 100 μL of MTT (5 mg/mL) was added to each well containing the cells, and the plates were again incubated (37 °C/4 h). After removing the culture medium, 100 μL of dimethyl sulfoxide was added to each well, and cell viability was determined at 570 nm in a microplate ELISA reader (Epoch-Biotek, Winooski, VT, USA). Figure 21 shows the adopted experimental procedure.

4.8. Alamar Blue Reduction Cytotoxicity Assay. In order to confirm the cytotoxic effect of the Sn−Cu−Zn and Sn−Ni−Zn alloys against the 3T3 cell line, the Alamar Blue colorimetric method[43] was used, which contains a redox indicator that, in the presence of metabolically active cells, changes from the oxidized form (blue and non-fluorescent) to the reduced form (pink and fluorescent). For this, cells (3×10^4 cells/well) were cultured in 96-well plates for 1 h for adhesion. Then, the medium was aspirated, and the cells were treated with metallic alloys at different concentrations for 24 and 48 h at 37 °C and 5% CO_2. After the metallic alloy was added, Alamar Blue was added in an amount equal to 10% of the medium volume contained in each well and the plate was incubated for 4 h at 37 °C and 5% CO_2. Then, the amount of reduced Alamar Blue was monitored by absorbance at 570 and 600 nm in an ELISA microplate reader (Epoch-Biotek, Winooski, VT, USA). Figure 22 shows the procedure adopted.

Our research team recently published another article that focuses on a commercially significant alloy, namely, Sn-0.7 Cu.[44] Complementary findings to the current results can be examined in this reference. It is crucial to emphasize that the Sn-0.2 Ni alloy constitutes an entirely distinct alloy system as compared to Sn−Cu. The Sn−Cu and Sn−Ni alloy systems exhibit different properties and applications, rendering it appropriate to study them separately due to their wholly distinct characteristics during solidification and processing as well as properties.

AUTHOR INFORMATION

Corresponding Author

José Eduardo Spinelli − *Department of Materials Engineering, Federal University of São Carlos (UFSCar), São Carlos 13565-905 São Paulo, Brazil;* orcid.org/0000-0003-0611-1038; Phone: +55 (16) 3351-8512; Email: spinelli@ufscar.br

Authors

Jeverton Laureano Paixão − *Department of Materials Engineering, Federal University of Rio Grande do Norte (UFRN), Natal 59078-970 Rio Grande do Norte, Brazil;* orcid.org/0000-0003-3482-2638

Raí Batista de Sousa − *Department of Materials Engineering, Federal University of Rio Grande do Norte (UFRN), Natal 59078-970 Rio Grande do Norte, Brazil*

Pâmella Raffaela Dantas de Freitas − *Department of Materials Engineering, Federal University of Rio Grande do Norte (UFRN), Natal 59078-970 Rio Grande do Norte, Brazil*

Rubiamara Mauricio de Sousa − *Department of Clinical and Toxicological Analyses, UFRN, Natal 59078-970 Rio Grande do Norte, Brazil*

Jefferson Romáryo Duarte da Luz − *Organic Chemistry and Biochemistry Laboratory, State University of Amapá (UEAP), Macapá 68900-070 Amapá, Brazil*

Bismarck Luiz Silva − *Department of Materials Engineering, Federal University of Rio Grande do Norte (UFRN), Natal 59078-970 Rio Grande do Norte, Brazil;* orcid.org/0000-0001-7191-1942

Complete contact information is available at: https://pubs.acs.org/10.1021/acsomega.3c06305

Notes

The authors declare no competing financial interest.

ACKNOWLEDGMENTS

The authors thank the support provided by FAPESP-São Paulo Research Foundation, Brazil (grants # 2019/23673-7 and # 2021/08436-9); Capes-Coordenação de Aperfeiçoamento de Pessoal de Nível Superior, Brazil (Funding Code 001); and CNPq-National Council for Scientific and Technological Development, Brazil.

REFERENCES

(1) Cheng, S.; Huang, C.-M.; Pecht, M. A review of lead-free solders for electronics applications. *Microelectron. Reliab.* **2017**, *75*, 77−95.

(2) Abtew, M.; Selvaduray, G. Lead-free solders in microelectronics. *Mater. Sci. Eng., R* **2000**, *27* (5−6), 95−141.

(3) Handwerker, C.; Kattner, U.; Moon, K. Materials science concepts in lead-free soldering. *Lead-Free Soldering in Electronics—Science, Technology and Environmental Impact*; CRC Press, 2003; pp 19−48.

(4) Cruz, C. B. d.; Kakitani, R.; Xavierb, M. G. C.; Silva, B. L.; Garcia, A.; Cheung, N.; Spinelli, J. E. Transient unidirectional solidification, microstructure and intermetallics in Sn-Ni alloys. *Mater. Res.* **2018**, *21*..

(5) Xavier, M. G. C.; Silva, B. L.; Garcia, A.; Spinelli, J. E. High Cooling Rate, Regular and Plate Like Cells in Sn-Ni Solder Alloys. *Adv. Eng. Mater.* **2018**, *20* (7), 1701179.

(6) Kong, Y.; Shao, J.; Wang, W.; Liu, Q.; Chen, Z. Electroless Sn-Ni alloy plating with high Sn content free of activation pretreatment. *J. Alloys Compd.* **2009**, *477* (1−2), 328−332.

(7) Belyakov, S. A.; Gourlay, C. M. NiSn4 formation during the solidification of Sn-Ni alloys. *Intermetallics* **2012**, *25*, 48−59.

(8) Wang, C.; Shen, H. Effects of Ni addition on the interfacial reactions between Sn-Cu solders and Ni substrate. *Intermetallics* **2010**, *18* (4), 616−622.

(9) Silva, B. L.; Cheung, N.; Garcia, A.; Spinelli, J. E. Thermal parameters, microstructure, and mechanical properties of directionally solidified Sn-0.7 wt.%Cu solder alloys containing 0 ppm to 1000 ppm Ni. *J. Electron. Mater.* **2013**, *42* (1), 179−191.

(10) Fan, J.; Liu, Z.; Zhai, H.; Wang, X.; Wang, Y.; Li, Y.; Zhou, X.; Wu, S.; Liu, J. Effect of Co content on the microstructure, spreadability, conductivity and corrosion resistance of Sn-0.7 Cu alloy. *Microelectron. Reliab.* **2020**, *107*, 113615.

(11) Schmetterer, C.; Flandorfer, H.; Richter, K. W.; Saeed, U.; Kauffman, M.; Roussel, P.; Ipser, H. A new investigation of the system Ni-Sn. *Intermetallics* **2007**, *15* (7), 869−884.

(12) Nogita, K. Stabilisation of Cu6Sn5 by Ni in Sn-0.7 Cu-0.05 Ni lead-free solder alloys. *Intermetallics* **2010**, *18* (1), 145−149.

(13) Zeng, G.; McDonald, S. D.; Gu, Q.; Terada, Y.; Uesugi, K.; Yasuda, H.; Nogita, K. The influence of Ni and Zn additions on microstructure and phase transformations in Sn-0.7 Cu/Cu solder joints. *Acta Mater.* **2015**, *83*, 357−371.

(14) Cho, M. G.; Kang, S. K.; Shih, D.-Y.; Lee, H. M. Effects of minor additions of Zn on interfacial reactions of Sn-Ag-Cu and Sn-Cu solders with various Cu substrates during thermal aging. *J. Electron. Mater.* **2007**, *36*, 1501−1509.

(15) Wang, F.; Ma, X.; Qian, Y. Improvement of microstructure and interface structure of eutectic Sn-0.7 Cu solder with small amount of Zn addition. *Scr. Mater.* **2005**, *53* (6), 699−702.

(16) Milheiro, A.; Nozaki, K.; Kleverlaan, C. J.; Muris, J.; Miura, H.; Feilzer, A. J. In vitro cytotoxicity of metallic ions released from dental alloys. *Odontology* **2016**, *104*, 136−142.

(17) Elshahawy, W. M.; Watanabe, I.; Kramer, P. In vitro cytotoxicity evaluation of elemental ions released from different prosthodontic materials. *Dent. Mater.* **2009**, *25* (12), 1551−1555.
(18) Ku, A., Oetinscitan, O., Saphores, J.-D., Shapirod, A., Schoenunp, J. M. Lead-free solders. issues of toxicity, availability and impacts of extraction. *Electronic Components and Technology Conference*, 2003; pp 47−53.
(19) Freitas, M. P.; Oshima, H. M.; Menezes, L. M. Release of toxic ions from silver solder used in orthodontics: an in-situ evaluation. *Am. J. Orthod. Dentofacial Orthop.* **2011**, *140*, 177−181.
(20) Hatim, N.; Jameel, N.; Mohammed, A. Biocompatibility of Soldering Materials Used for Repair of Cobalt Chromium Joints. *Rafidain Dent. J.* **2012**, *13*, 7−13.
(21) Bobzin, K.; Lugscheider, E.; Ernst, F.; Rösing, J.; Ferrara, S. Challenging gold based filler metals for uses in medicine. *Mater. Sci. Technol.* **2009**, *25*, 1422−1431.
(22) Barrett, C. S.; Massalski, T. B. *Structure of Metals. Crystallographic Methods, Principles and Data*; Pergamon, 1980.
(23) Degtyareva, V. F.; Sakharov, M. K.; Novokhatskaya, N. I.; Degtyareva, O.; Dera, P.; Mao, H. K.; Hemley, R. J. Stability of hume-rothery phases in Cu- Zn alloys at pressures up to 50 GPa. *Metall. Mater. Trans. A* **2006**, *37*, 3381−3385.
(24) Mizutani, U.; Takeuchi, T.; Sato, H. Interpretation of the Hume-Rothery rule in complex electron compounds: γ-phase Cu5Zn8 Alloy, FK-type Al30Mg40Zn30 and MI-type Al68Cu7Ru17Si8 1/1−1/1−1/1 approximants. *Prog. Mater. Sci.* **2004**, *49* (3−4), 227−261.
(25) Wang, F.; Wang, X.; Lv, Z.; Hang, C.; Chen, H.; Li, M. A novel antioxidant and low-temperature Sn-Zn solder paste based on Zn@ Sn core-shell structure. *Mater. Today Commun.* **2022**, *31*, 103356.
(26) Xavier, M. G. C.; Cruz, C. B.; Kakitani, R.; Silva, B. L.; Garcia, A.; Cheung, N.; Spinelli, J. E. Directional solidification of a Sn-0.2 Ni solder alloy in water-cooled copper and steel molds: Related effects on the matrix micromorphology, nature of intermetallics and tensile properties. *J. Alloys Compd.* **2017**, *723*, 1039−1052.
(27) Sobral, B. S.; Vieira, P. S.; Lima, T. S.; Spinelli, J. E.; Cheung, N.; Garcia, A.; Silva, B. L. Effects of Zn Addition on Dendritic/Cellular Growth, Phase Formation, and Hardness of a Sn-3.5 wt% Ag Solder Alloy. *Adv. Eng. Mater.* **2023**, *25* (6), 2201270.
(28) Ji, H.; Li, M.; Ma, S.; Li, M. Ni3Sn4-composed die bonded interface rapidly formed by ultrasonic-assisted soldering of Sn/Ni solder paste for high-temperature power device packaging. *Mater. Des.* **2016**, *108*, 590−596.
(29) Lin, C.-Y.; Jao, C.-C.; Lee, C.; Yen, Y.-W. The effect of non-reactive alloying elements on the growth kinetics of the intermetallic compound between liquid Sn-based eutectic solders and Ni substrates. *J. Alloys Compd.* **2007**, *440* (1−2), 333−340.
(30) He, M.; Lau, W. H.; Qi, G.; Chen, Z. Intermetallic compound formation between Sn-3.5 Ag solder and Ni-based metallization during liquid state reaction. *Thin Solid Films* **2004**, *462−463*, 376−383.
(31) Li, D.; Liu, C.; Conway, P. P. Characteristics of intermetallics and micromechanical properties during thermal ageing of Sn-Ag-Cu flip-chip solder interconnects. *J. Mater. Sci. Eng. A* **2005**, *391* (1−2), 95−103.
(32) Soares, T.; Cruz, C.; Silva, B.; Brito, C.; Garcia, A.; Spinelli, J. E.; Cheung, N. Interplay of Wettability, Interfacial Reaction and Interfacial Thermal Conductance in Sn-0.7Cu Solder Alloy/Substrate Couples. *J. Electron. Mater.* **2020**, *49*, 173−187.
(33) Ng, W. C. W.; Sweatman, K.; Akaiwa, T.; Nishimura, T.; Sato, M.; Gourlay, C.; Belyakov, S.Dissolution in service of the copper substrate of solder joints. *IEEE 18th Electronics Packaging Technology Conference (EPTC)*, 2016; pp 388−393.
(34) Lin, Y.-W.; Lin, K.-L. The early stage dissolution of Ni and the nucleation of Ni-Sn intermetallic compound at the interface during the soldering of Sn-3.5 Ag on a Ni substrate. *J. Appl. Phys.* **2010**, *108* (6), 063536.
(35) Lin, Y.-W.; Lin, K.-L. Nucleation behaviors of the intermetallic compounds at the initial interfacial reaction between the liquid Sn3. 0Ag0. 5Cu solder and Ni substrate during reflow. *Intermetallics* **2013**, *32*, 6−11.
(36) Gourlay, C. M.; Belyakov, S. A.; Ma, Z. L.; Xian, J. W. Nucleation and growth of tin in Pb-free solder joints. *JOM* **2015**, *67*, 2383−2393.
(37) El-Daly, A. A.; El-Taher, A. M. Evolution of thermal property and creep resistance of Ni and Zn-doped Sn-2.0 Ag-0.5 Cu lead-free solders. *Mater. Des.* **2013**, *51*, 789−796.
(38) Nogita, K.; Mu, D.; McDonald, S. D.; Read, J.; Wu, Y. Q. Effect of Ni on phase stability and thermal expansion of Cu6-xNixSn5 (X= 0, 0.5, 1, 1.5 and 2). *Intermetallics* **2012**, *26*, 78−85.
(39) Yu, C.-Y.; Duh, J.-G. Stabilization of hexagonal Cu6 (Sn, Zn) 5 by minor Zn doping of Sn-based solder joints. *Scr. Mater.* **2011**, *65* (9), 783−786.
(40) Directive, E. U.; et al. Restriction of the use of certain hazardous substances in electrical and electronic equipment (RoHS). *Off. J. Eur. Communities* **2013**, *46*, 19−23.
(41) International, A. *ASTM E3−11 (2017): Standard Guide for Preparation of Metallographic Specimens*; ASTM International West Conshohocken: PA, 2017.
(42) Gündüz, M.; Çadırlı, E. Directional solidification of aluminium-copper alloys. *J. Mater. Sci. Eng. A* **2002**, *327* (2), 167−185.
(43) Luz, J. R. D. d.; Barbosa, E. A.; Nascimento, T. E. S. d.; Rezende, A. A. d.; Ururahy, M. A. G.; Brito, A. d. S.; Araujo-Silva, G.; López, J. A.; Almeida, M. d. G. Chemical characterization of flowers and leaf extracts obtained from Turnera subulata and their immunomodulatory effect on LPS-activated RAW 264.7 macrophages. *Molecules* **2022**, *27* (3), 1084.
(44) Paixão, J. L.; de Sousa, R. B.; Sobral, B. S.; de Sousa, R. M.; da Luz, J. R. D.; Spinelli, J. E.; Silva, B. L. Zn additions modifying microstructure, thermal parameters and cytotoxicity of Sn-0.7Cu eutectic solder alloys. *Mater. Charact.* **2023**, *205*, 113337.

https://doi.org/10.1021/acsomega.3c06305
ACS Omega 2024, 9, 8829−8845